Fermi National Accelerator Laboratory

FERMILAB-Conf-80/48-EXP
7160.118

MULTIPLICITY MEASUREMENTS IN HADRON REACTIONS AT 100 AND 175 GeV*

W. Aitkenhead, D. S. Barton, G. W. Brandenburg, W. Busza,
T. Dobrowolski, J. I. Friedman, H. W. Kendall, T. Lyons,
B. Nelson, L. Rosenson, W. Toy, R. Verdier, and L. Votta
Massachusetts Institute of Technology, Cambridge, Massachusetts 02139 USA

and

M. T. Chiaradia, C. DeMarzo, C. Favuzzi, G. Germinario,
L. Guerriero, P. LaVopa, G. Maggi, F. Posa,
G. Selvaggi, P. Spinelli, and F. Waldner
Istituto di Fisica and Istututo Nazionale di Fisica Nucleare, Bari, Italy

and

A. E. Brenner, D. C. Carey, J. E. Elias, P. H. Garbincius,
G. Mikenberg, and V. A. Polychronakos
Fermi National Accelerator Laboratory, Batavia, Illinois 60510 USA

and

R. Meunier
CERN, Geneva, Switzerland

and

D. Cutts, R. S. Dulude, R. E. Lanou, Jr., and J. T. Massimo
Brown University, Providence, Rhode Island 02912 USA

June 1980

*Submitted to the XX International Conference on High Energy Physics, Madison, Wisconsin, July, 1980

MULTIPLICITY MEASUREMENTS IN HADRON REACTIONS AT 100 AND 175 GeV

W. Aitkenhead, D.S. Barton, G.W. Brandenburg, W. Busza, T. Dobrowolski, J.I. Friedman, H.W. Kendall, T. Lyons, B. Nelson, L. Rosenson, W. Toy, R. Verdier, and L. Votta

Massachusetts Institute of Technology, Cambridge, Mass. 02139

and

M.T. Chiaradia, C. DeMarzo, C. Favuzzi, G. Germinario, L. Guerriero, P. LaVopa, G. Maggi, F. Posa, G. Selvaggi, P. Spinelli, and F. Waldner

Istituto di Fisica and Istituto Nazionale di Fisica Nucleare, Bari, Italy

and

A.E. Brenner, D.C. Carey, J.E. Elias, P.H. Garbincius, G. Mikenberg, and V.A. Polychronakos

Fermi National Accelerator Laboratory, Batavia, Illinois 60510

and

R. Meunier

CERN, Geneva, Switzerland

and

D. Cutts, R.S. Dulude, R.E. Lanou, Jr., and J.T. Massimo

Brown University, Providence, Rhode Island 02912

ABSTRACT

We have measured charged particle multiplicities in the reactions $a + p \to c + X$, where a and c are either $\pi^{\pm}$, $K^{\pm}$, p, or $\bar{p}$. The data were taken using the Fermilab Single Arm Spectrometer Facility and a non-magnetic vertex detector. The average number of charged secondaries and their angular distribution are studied as functions of x and p_T of the scattered particle, c. We also present data on the total charged multiplicity for the reactions $a + p \to X$.

June, 1980

Submitted to the XX International Conference on High Energy Physics, Madison, Wisconsin July, 1980.

MULTIPLICITY MEASUREMENTS IN HADRON REACTIONS AT 100 AND 175 GeV

W. Aitkenhead[a], D.S. Barton[b], G.W. Brandenburg, W. Busza, T. Dobrowolski[c], J.I. Friedman, H.W. Kendall, T. Lyons, B. Nelson, L. Rosenson, W. Toy[d], R. Verdier, and L. Votta[e]
Massachusetts Institute of Technology, Cambridge, Massachusetts

and

M.T. Chiaradia, C. DeMarzo, C. Favuzzi, G. Germinario, L. Guerriero, P. LaVopa, G. Maggi, F. Posa, G. Selvaggi, P. Spinelli, and F. Waldner
Istituto di Fisica and Istituto Nazionale di Fisica Nucleare, Bari, Italy

and

A.E. Brenner, D.C. Carey, J.E. Elias, P.H. Garbincius, G. Mikenberg[f], and V.A. Polychronakos[b]
Fermi National Accelerator Laboratory, Batavia, Illinois 60510

and

R. Meunier
CERN, Geneva, Switzerland

and

D. Cutts, R.S. Duludé, R.E. Lanou, Jr., and J.T. Massimo
Brown University, Providence, Rhode Island 02912

(a) Present address: U.S. Windpower, Burlington, Massachusetts.
(b) Present address: Brookhaven National Laboratory, Upton, New York 11973.
(c) Present address: C.E.N., SACLAY, Gif-sur-Yvette, France.
(d) Present address: Bell Laboratories, Holmdel, New Jersey 07733.
(e) Present address: Bell Laboratories, Denver, Colorado 80234.
(f) Present address: DESY, Hamburg, W. Germany.

I. INTRODUCTION

The study of single particle inclusive spectra provides insight into the underlying constituent structure of the interacting systems. For example, inelastic lepto-production experiments measure the quark structure functions for the target nucleons.[1] Both low and high p_t hadronic reactions study the quark-quark interaction and the methodology of quark confinement.[2,3,4] The coincidence study of the remaining particles left behind may provide further insight into the reaction mechanisms through correlations with the trigger particles with respect to multiplicities, angular distributions, momentum spectra, or flavors.

The Fermilab Single Arm Spectrometer facility, SAS, was used to study the multiplicities and angular distributions of the associated charged particles produced in hadronic interactions. A non-magnetic vertex detector surrounding a liquid hydrogen target was triggered by a single charged hadron detected in the Single Arm Spectrometer. The beamline and spectrometer instrumentation allowed complete identification of the incident and trigger hadrons, allowing simultaneous measurement for all reactions of the type

$$a + p \Rightarrow c + x$$

where a and c are any combination of $\pi^{\pm}$,$k^{\pm}$,p, and $\bar{p}$. Data were taken at incident momenta of ±100 Gev and ±175 Gev. The scattered trigger hadrons were measured over the Feynman-x range $0.2 \leq x \leq 0.94$ and transverse momentum range $0.1 \leq p_t \leq 1.2$ Gev/c. We present results on

the multiplicity and pseudo-rapidities of the remaining charged particles as a function of beam and trigger particle species and kinematics.

II. APPARATUS AND TECHNIQUES

A. Description

1. M6/SAS Single Particle Inclusive Cross Sections

The Fermilab M6 beamline and the Single Arm Spectrometer have been used by this group for a continued study of single particle inclusive elastic and inelastic hadronic scattering.[5] This facility provides events tagged with regard to beam and spectrometer particle momentum, direction, and position. Eight Cerenkov counters, electromagnetic and hadronic shower counters, and a muon absorber give unambiguous identification of the incident and scattered particles on an event-by-event basis. This information provides measurement of the single particle inclusive cross sections.[6] In addition, the M6/SAS system provided a fast trigger to the vertex detector to study properties of the charged particles associated with a fast forward hadron.

The single particle inclusive data reported here include studies of the beam fragmentation region, Feynman $x \geq 0.2$, for moderate transverse momenta $0.1 \leq p_t \leq 1.2$ GeV/c. All results are empty target substracted and are averaged over plus and minus

production angles in order to reduce systematic effects.

2. Transmission Total Cross Section Triggers

In addition to the spectrometer system described in Ref. 5, provision was included to form a total cross section trigger. This allowed the properties of the associated particles measured in this experiment with a minimal bias trigger to be compared with similar bubble chamber results. A small scintillation counter was placed at the momentum dispersed focus of the spectrometer. The spectrometer was placed at zero degrees to the incident beam and tuned to the beam momentum. Particles that met the criteria for beam particles, but failed to fire this scintillation counter, were candidates for inelastic interactions and produced a trigger for the vertex detector. The largest background for a total cross section measurement was from low t, high x scatters that struck the transmission veto counter. The effect of this background was estimated using the results of Ref. 5. Losses of transmission due to scattering or absorption in the spectrometer were treated as empty target backgrounds.

3. Vertex Detector[7]

The 20" liquid hydrogen target (0.06 absorption length) was surrounded by a non-magnetic vertex detector. The primary goal of this detector system was to measure the associated charged particle multiplicities and pseudo-rapidity distributions for single particle inclusive events triggered by the Single Arm Spectrometer. The vertex detector and liquid hydrogen target were mounted on a tilt frame to maintain alignment along the incident beam while the beam was pitched vertically to vary the p_t of the trigger reaction. A schematic layout showing the relative positions of the vertex detector components is shown in Fig. 1.

Three separate detector systems were used to cover the full angular range: the forward multiplicity Cerenkov counters (MC), the mid-range multiwire proportional chambers (PC), and the wide angle target recoil hodoscopes (MT and MB). All detectors had a hexagonal geometry. Two adjacent detector regions allowed substantial overlap for tracks originating from any vertex within the hydrogen target. Table I lists the detector properties.

The multiplicity Cerenkov counters, MC, detected

charged particles within 1.8° of the incident beam. Multiwire proportional chambers would not have been feasible for this region because of tracking ambiguities due to the large particle density for a large fraction of our events. The incident beam and spectrometer trigger particle also passed through the MC counters. This required short resolving times and high rate capability. An array of six one-half inch thick (0.02 absorption length) Pilot 425 Lucite Cerenkov Counters[8] was positioned on the incident beamline. The Cerenkov light output was independent of the velocity for particles with $\beta > 0.9$ allowing detection of multiple particles in a single MC counter by pulse height analysis. The MC array could be removed remotely to study backgrounds and absorption of the spectrometer trigger particles.

Multi-wire proportional chambers (PC) covered the angular range 1.5° to 24°. In addition to track counting, the PC array was used to reconstruct the interaction vertex position for each event, a necessary point for studying angular distributions for an extended target. The nine sense planes were arranged in three packages providing three points for each track in each of three projections rotated 120° between views.[9] There were 2600 sense wires of 0.080" spacing in the entire vertex detector.

Hexagonal kapton plugs of 0.002" thickness were used to deaden the beam region for the PC's. The plug sizes were chosen to shadow most of the MC array. The middle triplet package had a smaller plug to allow more overlap with the MC array for intercalibration studies.

The hexagonal target hodoscope (MT and MB) counters covered the region beyond 22°. The double layer of scintillators discriminated against delta rays while maintaining sensitivity to stopping protons. A coincidence between the inner (MT) and outer (MB) counters signaled a penetrating particle. Stopping recoil protons were detected by requiring a 6 times minimal energy deposition in the inner MT layer without requiring a MT.MB concidence. The MT counters formed three hexagonal barrels along the beam. Each set of three MT counters was backed up by a single MB counter for a total of eighteen MT and six MB counters.

The overall resolving time of the vertex detector was determined by the 40 nsec charge collection time of the multi-wire proportional chambers. For the multiplicity analysis, it was required that there be no other beam particle incident within ±3 RF buckets (±55 nsec) of the spectrometer trigger to minimize

backgrounds due to old tracks from events in nearby RF buckets. Events were vetoed if there were more than one beam particle in a bucket as detected by ambiguous beam Cerenkov patterns or large pulse heights in beam trigger counters. Such accidental rates and MWPC wire currents limited our luminosity to 1.5×10^5 interactions/second or 3×10^6 incident hadrons/second.

B. Analysis

The largest background for spectrometer triggers was produced by the MC array in Fig. 1. Interactions of the beam in this counter resulted in abnormally low multiplicities recorded in the vertex detector. The reconstructed beam and spectrometer trajectories were used to determine the z position (along the beam) of the interaction vertex and eliminate this background. In Fig. 2, the typical full and empty target vertex z distribution appears for a 3.5 mrad production angle at 60 GeV/c. The target is symmetric about 0 while the MC background peaks at 1.65 meters. The spectrometer triggers were required to have $z < 0.75$ meters.

For those spectrometer triggers which were completely reconstructed, satisfied all cuts and were completely

identified, the multi-wire proportional chamber data was decoded. The tracking algorithm first found a vertex by extrapolating hits in each projection back to the target. A fit combining all three projections determined the x,y,z coordinates of the interaction vertex. Tracks were discarded until an acceptable χ^2 was attained, and the discarded tracks were examined for a second vertex. Using thin nuclear targets, the PC vertex resolution was measured to be σ_z = 0.7 inch. After the vertex was determined, the three PC packages were analyzed beginning with the downstream package. Lines were drawn to the vertex including hits in other packages within a 4mm roadwidth. The found tracks were scanned, deleting the most ambiguous tracks which shared too many common projections. Two PC tracks within 6mm were treated as a single track.

Multiple particles could be detected in a single MC counter as evidenced by the pulse height spectrum shown in Fig. 3. The pulse height cuts corresponding to a specific number of particles were set by equating the miscounting of adjacent multiplicity bins in order to preserve the average multiplicity. In those cases where a single MC counter appeared to have more than three particles detected, it was assumed that a secondary interaction occured in the lucite counter and the true multiplicity for that counter was set to one. The percentage or good

events with more than three particles in a single MC counter was estimated to be much less that 1%.

Wide-angle particles were detected by a coincidence between the inner MT counter and the corresponding MB counter. A coincidence was not required for particles stopping in the inner counter provided there was at least a six times minimum energy deposition in the MT counter.

No vertex was found in 5-40% of the events depending on the spectrometer kinematic setting. For the triggers with large Feynman x, the small multiplicity gave a large probability of no PC tracks. As x decreased, the PC multiplicity increased enhancing the probability of finding the vertex. When no vertex was found, the center of the target was used to compute the track coordinates. The overall multiplicity and angular distribution for each event was determined by combining the results from the three vertex detector systems. Coincidences between the overlap regions of the individual detectors were checked to prevent double counting. The charged particle hit pattern for each reaction channel and kinematic setting was stored in six angular bins with respect to the beam axis. Fig. 1 and Table II list those bins and the corresponding pseudo-rapidity ranges. Empty target subtractions were performed on all distributions at this point.

C. Corrections[7,10]

For each reaction type, we measured a raw charged prong count N_{oj}. To extract the true charged prong count, N_{Ti}, we assume there is a linear transformation

$$N_{oj} = \sum_i M_{ji} N_{Ti}$$

where M_{ji} is the probability of an event with i charged prongs being measured as having j charged particles. The elements M_{ji} were determined using a Monte Carlo method which simulated events with both charged and neutral particles, including the vertex detector response.[10]

Two related methods were used to generate the hadron distribution at the vertex. Actual reconstructed Fermilab 30" bubble chamber events for 100 GeV pp interactions[11] were used for the charged tracks. Extra neutral tracks were generated using a p_t-limited phase space Monte Carlo method to balance momentum.[12] The number of extra neutrals was generated as a Poisson distribution using the average number of K°, π°, and Λ° measured in bubble chamber data.[13]

The second method involved generating both charged and neutral particles using the p_t-limited phase space Monte

Carlo. This method also generated events which were triggered by the detected spectrometer particle. The recoiling hadrons were generated for the appropriate missing mass M_x^2 and recoil momenta. The overall single particle distributions generated were constrained to reproduce the inclusive data measured by the spectrometer.

The generated events of a given multiplicity j were then propagated through our vertex detector taking the following effects into account: two or more particles in the same MT.MB counter, delta rays, multiple scattering, ionization energy loss, elastic and inelastic scattering, gamma ray conversion, and the decays of neutral particles. The measured detector inefficiencies, misalignments, and responses were also included in the program. The distribution in the number of the particles detected by our vertex detector produced the transform matrix

$$M_{ij} = \frac{\text{Number of j prong events detected as i prongs}}{\text{Number of simulated events with j prongs}}$$

The charged prong distribution N_{Tj} was calculated by least squares minimization of

$$\chi^2 = \sum_i \frac{(N_{oi} - M_{ij} N_{Tj})^2}{\sigma_i^2}$$

where σ_i is the statistical error on the number of events of apparent multiplicity i. A problem regarding the oscillation of the fitted charged prong coefficients was solved by constraining the prong count distribution

$$N_{Ti} = ae^{-bi}$$

for i greater than twice the average multiplicity. This form approximates the tail of the KNO scaling distribution discussed later. For rare channels, such as $\bar{p}p \to k^+X$, with less than 100 detected events, we simply used a correction ratio of (fitted <n>/raw<n>) determined for a much higher statistics process such as $\pi^-p \to \pi^+X$ to estimate the average multiplicity of the rare channel. A similar least squares matrix approach was used to correct the pseudo-rapidity distributions.

Three actual data sets were used to calibrate our Monte Carlo and detector models. Non-interactive beam particles produced delta rays in the hydrogen target. By studying the vertex detector response to these beam triggers, we directly observed the difficult to model major background due to production, self-absorption, multiple scattering and transport of very low energy electrons through our hydrogen target and detector. Elastic scattering data was used to calibrate the response of the MT and MB counters

to slow recoil protons. Finally, we required good agreement with the total inelastic multiplicities observed in bubble chambers as described in Section III-A.

III. TOTAL INELASTIC CROSS SECTION STUDIES

As a calibration of the vertex detector, the spectrometer transmission veto system formed a total cross section trigger. Total inelastic charged multiplicity data were compared to bubble chamber measurements in order to check detector performance and to understand systematic differences. This section contains measurements of the total inelastic cross sections, the mean inelastic charged multiplicities, and the topological cross sections for $\pi^{\pm}$, $k^{\pm}$, p and $\bar{p}$ beams at 100 and 175 GeV/c. The negative beam data were used to demonstrate KNO scaling.

A. Total Cross Sections

The total cross sections measured in this experiment are listed in Table III. These were corrected for elastic events vetoed by the spectrometer[5] ($\sim$20% and 50% at 100 and 175 GeV/c respectively) as well as for the loss of low-t ($|t| \leq 0.04$ GeV^2) inelastic diffractive events[14]. These data are compared to those of Carrol, et. al.[15] The quoted errors are statistical only. The systematic error is estimated to be about 3%. The largest source of error is the uncertainty in the spectrometer acceptance for the elastic cross section ($\leq$ 1.5%). Other sources of error include beam doubles ($\leq$ 0.5%), beam particle misidentification ($\leq$ .1%) and muon and electron contamination of the pion sample ($\sim$5%).

B. Mean Inelastic Multiplicities and Charged Topological Cross Sections

A comparison of the mean multiplicities of charged particles measured in this experiment with those measured with bubble chambers appears in Table IV. The quoted errors are only statistical. Systematic errors are discussed later. Although intended as a calibration, for some channels this data represent the first multiplicity measurements at these energies.

The topological cross sections for $\pi^+ p$,pp and $\bar{p}p$ at 100 GeV/c are listed in Table V indicating good agreement with bubble chamber measurements. Topological cross sections of the remaining channels are given in Table VI. For ease of comparison, the topological cross sections in these tables have been normalized to the inelastic cross sections of Ref. 5 and 15.

C. Scaling

Charged topological cross sections for incident hadrons have been shown to obey KNO scaling.[16] The 100 and 175 GeV/c negative beam topological cross sections have been plotted as $\langle n \rangle \sigma_n / \sigma_{inelastic}$ vs. $n/\langle n \rangle$ (Fig. 4). Our data is in good agreement with the curve, which represents a

KNO fit[17] to pp data over the range 50 to 300 GeV/c. This is the first demonstration of KNO scaling for negatively charged hadron beams.

D. Corrections and Estimates of Systematic Error

These are two sources of systematic error for the total inelastic multiplicities and topological cross sections. Uncertainty in the elastic event substraction can contaminate the two-prong topology and shift the average multiplicity by about 0.06 charged particle. The other source of systematic error is in the modeling of the detector system and in the parameterization of neutral particle production and backgrounds used in the Monte Carlo program. The set of physical effects considered and the detector system modeling were discussed in Section II. Table VII summarizes each effect, together with the actual corrections applied to the 100 GeV π^-p data. For all reactions, the systematic uncertainty in the average charged multiplicity is $\leq$3% of the multiplicity. The understanding and treatment of this source of error are directly applicable to the associated multiplicity data.

IV. ASSOCIATED CHARGED PARTICLE MULTIPLICITIES

A. Kinematic Variables and Data Presentation

In this experiment, typical data runs consisted of varying the scattering angle at a constant spectrometer momentum setting. Over all of the kinematic range covered, the ratio $x = P_{spectrometer}/P_{beam}$ approximated Feynman-x to better than 2% accuracy. For each spectrometer momentum, angle settings corresponding to p_t = 0.3, 0.5, 0.75 GeV/c were chosen. Additional p_t values out to p_t = 1.2 GeV/c were covered for x = 0.3, 0.6, and 0.92 or 0.94.

The most useful kinematic variables for studying associated multiplicities in the reaction a + p → c + X are the total missing mass squared M_x^2 and the invariant momentum transfer t defined as

$$M_x^2 = (\vec{P}_a + \vec{P}_b - \vec{P}_c)^2 \approx s(1-x)$$

$$t = (\vec{P}_a - \vec{P}_c)^2 \approx M_a^2(1-x) + M_c^2\left(1-\frac{1}{x}\right) - P_t^2/x$$

where $s = 2M_p P_{beam}$, the total energy squared. These forms are approximations valid at high energies.

The average associated charged multiplicities for selected channels are shown as functions of t and x in Figs. 5 and 6. Complete tables of these results for all reaction channels are available in Ref. 7.

B. t-dependence of the Leading Particle Associated Multiplicities

previous bubble chamber [18,19] and counter experiments [20,21] have studied the M_x^2 and t-dependences of the associated multiplicities in leading particle reactions of the type

$pp \rightarrow pX^-$
$\pi^- p \rightarrow \pi^- X$

$\pi^- p \rightarrow Xp$

Most of these pp → pX experiments find very little dependence of the multiplicity on the momentum transfer t. However, the ARGO group[21] found definite increase in the associated multiplicity with increasing t consistent with a form $\bar{n} = \alpha(x) + \beta'(M_x - M_p)^2 |t|$. The Fermilab 30" bubble chamber group[19] has also found a form $\bar{n} = \alpha(x) + \beta|t|$ for the reaction $\pi^- p \rightarrow \pi^- X$ where t coefficient i s independent of x or M_x^-.

The leading particle data of this experiment have been fit to the form

$$\bar{n}(x,t) = \alpha(x) - \beta(x)\, t$$

at a constant x or M_x^2. Results of this fit are displayed in Fig. 7. For the high statistics channels, the term $\beta(x)$ is positive, indicating an increase in the average multiplicity with increasing scattering angle. $\beta(x)$ is independent of x except for $x > 0.8$, where it falls to zero as $x \rightarrow 1$ in a manner consistent with the ARGO spectrometer data.[21] The t slopes obtained for $\pi^{\pm} p \rightarrow \pi^{\pm} X$ are somewhat smaller than those of Ref. 19, where a constant $\beta = 1.15 \pm 0.18$ was used for all x.

C. M_x^2-Dependence

The parameters $\alpha(x)$ in the previous fit, which represent the average multiplicity at $t = 0$, are plotted for two reactions in Figs. 8 and 9. This removes any complications due to t_{min} effects. For the $pp \to pX$ case, the dotted curve represents ISR data of Albrow et al.[20] as well as an average of the 100-400 GeV bubble chamber data.[19] This curve agrees well with our data and is also a good representation of the s-dependence of the $pp \to X$ inelastic multiplicities. On the other hand, the $\ell n M_x^2$ slope of our $\pi^{\pm}p \to \pi^{\pm}X$ data is somewhat shallower than either the $pp \to pX$ multiplicities or that of Ref. 19. These data more nearly follow the s-dependence of the $\pi^{\pm}p \to X$ multiplicities. Assuming a single exchange trajectory for $hp \to hX$ at high x or low M_x^2, one would expect identical behavior for associated multiplicities for all hadrons h, since all target fragments arise at the pomeron-proton vertex.

Fig. 10 shows the average multiplicities for several reactions at $t = 0$ and $M_x^2 = 53$ GeV^2. The results for these reactions are essentially the same with an average $\bar{n} = 4.62$, and a standard deviation, $\sigma = 0.18$, and they agree well with the bubble chamber[19] results for $pp \to pX$, $\Lambda^{o}X$, and $\Delta^{++}X$. This shows that at fairly low M_x^2 the multiplicity is quite independent of the exchanged particle, whether Pomeron, meson, or baryon, and primarily depends on M_x^2.

Fig. 11 shows the average associated multiplicities for various channels at $M_x^2 = 131$ GeV and $t = 0$. There is considerably more scatter in the data ($\sigma = 0.6$) than for Fig. 10. This is not surprising since at this x-value the spectrometer trigger particle may be centrally produced instead of being a true beam fragment.

D. Global Fit

A form $\bar{n}(M_x^2,t) = A + B \ln M_x^2 + C |t|$ was used to parameterize all channels where there was sufficient data at at least 10 kinematic settings. This form includes a $\ln M_x^2$ term representing the growth of the available rapidity space and a $|t|$ term which arises from Regge-ology.[22] The fitted values are presented in Table VIII. The results of these fits have been indicated as solid curves in Figs. 5-9. The coefficients show good agreement with previous experiments except for the non-vanishing t-dependence for $pp \rightarrow pX$ observed in this experiment. The channels where the incoming and outgoing particles differ show little or no t-dependence.

The $\ln M_x^2$ coefficients, B, for all leading channels $hp \rightarrow hX$ are compared with the $\ln s$ term for $hp \rightarrow X$ inelastic multiplicities[19] Fig. 12. Good agreement is observed between the channels with the same incident positive beam. The negative beam results for the associated multiplicity are approximately two standard deviations lower than the corresponding inelastic multiplicities.

V. ANGULAR DISTRIBUTIONS FOR THE ASSOCIATED PARTICLES

A. Introduction

The CHLM group[20] has studied the associated multiplicities and angular distributions for pp interactions at the ISR. Pseudo-rapidity distributions for $pp \to \pi^{\pm}, K^{\pm}, p, \bar{p}X$ triggers show a flat central plateau for the recoil system. The shape and cutoff of the rapidity spectra near the edges of the recoil system phase space are independent of the mass of the recoil system. The longitudinal and angular distributions are consistant with those expected for a p_t-limited phase space model.

Due to limited statistics, all angular distributions for this experiment have been integrated over azimuthal angle and number of charged particles. We will discuss the behavior of the pseudo-rapidity spectrum as a function of x for leading particle interactions. The correlation information for OPE ρ° production will be discussed in more detail. Finally, fragmentation models are compared with the angular distributions. The study of such correlation data may provide an extra handle on theoretical understanding of production and fragmentation processes.

In the absence of momentum analysis, the associated particles are described by the pseudo-rapidity.

$$\eta_{lab} = -\ln \tan (\theta/2)$$

where θ is the production angle relative to the beam direction. At high energies, this approximates the rapidity except for very forward or backward particles. In particular, η diverges as $\theta \to 0°$ or 180°. Assuming all particles have p_t=0.3 GeV, a typical average transverse momentum, the maximum pseudo-rapidity available to an associated particle is:

$$\eta_{MAX} \sim \ln \frac{2P_0(1-x)}{\langle p_t \rangle}$$

where p_o is the beam momentum and x is the Feynman-x of the trigger hadron. This estimate works reasonably well to define the η-bin center and bin width corresponding to the MC detector region. Similarly, for backward particles $\eta_{min} \sim -1.1$, independent of x or p_o.

B. Particles Associated With Leading Hadrons

The pseudo-rapidities of particles produced in the reaction $\pi^- p \to \pi^- X$ at 175 GeV and p_t=0.5 GeV/c are depicted in Fig. 13. As the x-value of the trigger π^- decreases, the width of the pseudo-rapidity spectrum increases as $\ln M_x^2$ as expected. The $\eta \sim 0$ region and the forward slope are independent of x. The dotted line represents the

average slope observed by Ref. 20. Finally, a central rapidity plateau develops.

Fig. 14 shows the relationship between the total and associated rapidity distributions at a common $s=M_X^2 = 192$ GeV^2. The associated η-distribution for $pp\rightarrow pX$ measured in this experiment (histogram) is compared to the total η-distributions for $pp\rightarrow X$ (Ref. 23) and $\bar{p}p\rightarrow X$ (Ref. 24) at 100 GeV. Good agreement is attained for all three data sets indicating that these processes can all be described by a simple p_t-limited phase space model.

C. Resonance Production

The process $\pi^{\pm}p\rightarrow\pi^{+}X$ at high Feynman-x[25] exhibits many features not described by phase space. Strong correlations are expected for the production and decay of ρ° mesons. The $\pi^{\pm}\rightarrow\pi^{\mp}$ channel is compared to the conventional fragmentation $p\rightarrow\pi^{-}$. Fig. 15a shows the extra cross sections at high x due to forward resonance production and decay for the pion beam. The $p\rightarrow\pi^{-}$ and $\pi^{+}\rightarrow\pi^{-}$ associated multiplicities are similar as a function of x. In Fig. 15c, the parameter $f_2 = \langle n^2\rangle-\langle n\rangle^2-\langle n\rangle$ indicates that the multiplicity distribution is much narrower than Poisson for the $\pi^{+}\rightarrow\pi^{-}$ channel at high x. Fig. 15d,e show the inclusive cross section for a given

number of charged prongs. For $\pi^+ \rightarrow \pi^-$, the 3- and 5-prong cross sections are flat above x=0.5 whereas all prong cross sections fall rapidly for $p \rightarrow \pi^-$. The resonance contribution consists primarily of 2 and 4 prong events at the exchanged $\pi^+ p$ vertex in Fig. 15f.

The associated charged particle pseudo-rapidity distributions are shown in Fig. 15g. As the spectrometer trigger π^- increases in momentum above x=0.3, the phase space plateau narrows and a very large positive correlation emerges at $n \sim 4$. This represents the π^+ from the ρ° decay.

D. Correlations in Fragmentation Models

The fragmentation of particle a into particle c at high Feynman x has been theoretically described in terms of constituent interchange and recombination models.[3,4] For many reaction channels, a single beam particle valence quark ends up in the forward hadron. The remaining valence quarks in a may be exchanged with the target system or may continue forward, possessing the remaining momentum of the incident hadron. The latter situation should be manifested in additional high rapidity secondary hadrons produced by the possibly fast spectator quarks.

Correlations between the trigger hadron species and the associated charged particle multiplicities in the angular range $\eta \geq 3.3$ were studied for meson fragmentation reactions. The spectrometer trigger hadron was required to have x=0.88. As shown in Fig. 15g, this kinematic combination allowed clean separation of fast forward beam fragments from the slower, wide-angle target fragments. Pseudo-rapidity distributions for leading particle channels hp→hX are dominated by target fragments and provided a measure of the average associated multiplicity of about 0.5 particles for $\eta \geq 3.3$. The excess multiplicity above this tail of the target fragmentation region is presented in Fig. 16. Assuming an average p_t of 0.3 GeV/c, an additional beam fragment may have up to η=4.4, consistent with both the remaining beam hadron momentum and the average x-value determined by the hadron structure functions.

For most channels, the excess multiplicity for η>3.3 is consistant with zero. It should be noted that the minimal number of spectator quarks is at most two for these channels. The double charge exchange reactions $\pi^{\pm} \rightarrow \pi^{\mp}$ or $K^{\mp}$ do have an excess forward multiplicity, but this presumably results from resonance production. The beam and spectrometer particles share no quarks in common and require at least three spectator quarks. Reactions such as $p \rightarrow k^{-}$ or $p \rightarrow \bar{p}$ may tend to have similar higher forward

multiplicities. However, the cross sections are vanishingly small in the high x region where beam and target fragments could be separated in the angular distributions.

VI. Summary and Conclusions

This experiment studied the charged particle multiplicities and angular distributions in hadronic interactions using both inelastic cross section and forward spectrometer triggers. To a high degree, these quantities agree with those expected from p_t-limited longitudinal phase space models.

The multiplicities behave as

$$\bar{n} = A + B \ln M_x^2$$

or

$$\bar{n} = A + B \ln s$$

where the coefficients are independent of particle species or kinematics implying that the available energy s or M_x^2 is most important for understanding multiplicities. A linear t-dependence was observed for the leading channels $pp \to px$, $\pi^{\pm}p \to \pi^{\pm}X$. The coefficient of t was constant for $x<0.8$, but decreased to zero as $x \to 1$. The multiplicities and angular distributions for particle exchange reactions were similar to those for leading particles at an equivalent M_x^2 except for the effects of forward resonance production.

A more extensive discussion and more complete tables of these results can be found in Ref. 7.

We would like to express our thanks to the many people at Fermilab who have contributed to the successful operation of the Single Arm Spectrometer and of the accelerator. This work was supported in part by the U. S. Department of Energy under Contract Numbers EY76-C-02-3000 (Fermilab), 3069 (MIT), 3130 (Brown), and the Istituto Nazionale de Fisica Nucleare (Italy).

REFERENCES

1. A. Bodek, et al., Phys. Rev. D20, 1471 (1979).
2. R. P. Feynman, R. D. Field, G. C. Fox, Phys. Rev., D19, 3320 (1978)
3. K. P. Das and R. C. Hwa, Phys Lett., 68B, 459 (1977).
4. S. J. Brodsky and J. F. Gunion, Phys. Rev. D17, 848 (1978).
5. D. S. Ayers, et al., Phys. Rev. D15, 3105 (1977).
6. D. Cutts, et al., Phys. Rev. Lett., 43, 319 (1979).
   W. Aitkenhead, Fermilab-Pub. 80/32 (1980) submitted to Phys. Rev. Lett.
7. L. G. Votta, Ph.D. Thesis, LNS-MIT (1979), unpublished.
8. P. H. Garbincius, Nucl. Inst. Meth., 131, 273 (1978).
   and also described in Ref. 23.
9. E. F. Anelli, Rev. Sci. Instrum., 49, 1054 (1978).
10. B. G. Gibbard, et al., Phys. Rev. D11, 2367 (1975),
    used a similar matrix unfolding procedure.
11. T. Ferbel, private communication of reconstructed bubble chamber events as described by J. W. Chapman, et.al., Phys. Lett., 47B 465 (1973).
12. D. C. Carey, Monte Carlo Phase Space with Limited Transverse Momentum, Fermilab-Pub, 77/43 (1977) unpublished.
13. S. Kahn, APS/DPF, Seattle, 1975, p 292.
14. R. L. Anderson, et al., Phys. Rev. Lett., 38, 880 (1977).
15. A. Carrol, et al., Phys. Rev. Lett., 33, 928 (1974) and 33, 932 (1974).
16. G. Giacomelli, Proc. 19th Int. Conf. on HEP, Tokyo, Japan (1978) p53.
    Z. Koba, et al., Nucl. Phys. B40, 317 (1972).
17. P. Slattery, et al., Phys. Rev. Lett., 29, 1624 (1972).
18. J. Whitmore, Physics Reports, 5C, 273 (1974) and Physics Reports, 27C, 187 (1976).

19. D. Brick, et al., Phys. Rev., D19, 743 (1979) and references listed therein.

20. M. G. Albrow, et al., Nucl. Phys. B102, 275 (1976).

21. A. Ramanauskas, Phys. Rev. Lett., 31, 1371 (1973).
T. S. Clifford, et al., Phys. Rev. Lett., 33, 1239 (1974).
W. N. Schreiner, Ph.D. Thesis, VPI, 1973, unpublished.

22. C. deTar, Phys. Rev., D17, 879 (1978).

23. J. E. Elias, et al., Fermilab-Pub, 79/47 (1979), to be published in Phys. Rev.

24. R. Raja, $\bar{p}p \to X$ data set, private communication.

25. D. Cutts, et al., Phys. Rev. Lett., 40, 141 (1978).

26. W. M. Morse, et al., Phys. Rev., D15, 66 (1977).

27. E. L. Berger, et al., Nucl. Phys., B77, 365 (1974).

28. R. E. Ansorge, et al., Phys. Lett., 59B, 299 (1975).

29. V, E. Barnes, et al., Phys. Rev. Lett., 34, 415 (1975).

30. D. Fong, et al., Nucl. Phys. B102, 386 (1976).

Table I

Multiplicity Detector Details

Counter	z Position*	Type of Light Detected	Element Size
MC1 - 6	67.9"	Cerenkov	2.0" (on a side, equilateral triangle)
MT1 - 6	-5.0"	Scintillation	8.5" x 10."
MT7 - 12	+5.0"	Scintillation	8.5" x 10."
MT3 - 18	+15.0"	Scintillation	8.5" x 10."
MB1 - 6	+5.0"	Scintillation	8.5" x 30."
HTC	68.4"	Scintillation	Hole Trigger Counter

Multiwire Proportional Chambers

Sense Plane	z Position*	Plug Size	Coordinate Measured**
PC11	25.1"	1.5" x 1.8"	u_1
PC12	24.5"	1.5" x 1.8"	u_2
PC13	23.9"	1.5" x 1.8"	u_3
PC21	45.8"	1.0" x 1.2"	u_1
PC22	45.2"	1.0" x 1.2"	u_2
PC23	44.6"	1.0" x 1.2"	u_3
PC31	63.6"	3.3" x 3.8"	u_1
PC32	63.0"	3.3" x 3.8"	u_2
PC33	62.4"	3.3" x 3.8"	u_3

*All z positions are given relative to the center of the 20" Hydrogen target which is at a z = 1470', downstream of the meson production target.

Table II

Charged Multiplicity Detector Angular Bins

Bin Name	Detector Req.	ϕ_{min} (rad)	ϕ_{max} (rad)	η_{min}	η^*_{max}	$\delta\eta$
η_1	MC	0	.0366	4.00	∞	
η_2	PC3A	.0366	.0737	3.30	4.00	.7
η_3	PC3B	.0737	.1342	2.70	3.30	.6
η_4	PC21	.1342	.2437	2.10	2.70	.6
η_5	PCNT	.2437	.4836	1.40	2.10	.7
η_6	MT	.4836	∞	∞	1.40	

Table III

Total Cross Sections (mb)

	π^+p	K^+p	pp	π^-p	K^-p	$\bar{p}p$
Beam Momentum = 100 GeV/c						
Measured						
σ	22.1± .9	17.7±1.6	36.7±1.3	23.1± .7	20.2±1.1	38.1±1.1
Corrections						
$\sigma_{elastic}$	.7± .2	.5± .1	1.7± .3	.7± .1	.5± .2	2.0± .4
$\sigma_{inelastic}$	.1± .1	.1± .1	.3± .1	.1± .1	.1± .1	.3± .1
Corrected Result						
σ_{total}	23.4± .9	18.4±1.7	38.7±1.3	23.9± .7	20.8±1.2	40.4±1.2
World Data						
σ^{*}_{total}	23.3± .1	18.9± .1	38.4± .1	24.0± .1	20.4± .1	42.0± .2
$\sigma^{**}_{elastic}$	3.3± .2	2.5± .1	7.1± .4	3.3± .1	2.5± .1	7.8± .6
Beam Momentum = 175 GeV/c						
Measured						
σ	20.9±1.1	16.9±1.6	23.9±1.0	21.3± .8	20.1±1.0	36.2±1.6
Corrections						
$\sigma_{elastic}$	1.6± .2	1.1± .3	3.7± .3	1.7± .2	1.1± .2	4.0± .6
$\sigma_{inelastic}$	.4± .1	.2± .1	1.0± .2	.4± .2	.3± .1	1.0± .3
Corrected Result						
σ_{total}	22.9±1.2	18.2±1.8	39.6±1.1	23.4± .8	21.4±1.1	41.2±1.7
World Data						
σ^{*}_{total}	23.6± .1	19.6± .1	38.8± .1	24.2± .1	20.7± .1	41.6± .5
$\sigma^{**}_{elastic}$	3.4± .1	2.5± .1	7.1± .3	3.4± .1	2.6± .1	7.1± .5

* ref. 14.

** ref. 15.

*** ref. 5.

Table IV

Mean Inelastic Charged Multiplicity

Reaction	Incident Beam Momentum (GeV/c)	This Experiment Mean	D	No. of Events	Mean	D	Ref
π^+p	100	6.75 ± .16	3.33 ± .12	2186 ± 116	6.62 ± .07	3.19 ± .05	26
π^-p	100	6.79 ± .11	3.15 ± .08	3461 ± 140	6.79 ± .08	3.39 ± .04	27
π^+p	175	7.55 ± .21	3.67 ± .14	1210 ± 72			
π^-p	175	7.83 ± .14	3.81 ± .10	2013 ± 80			
K^+p	100	6.95 ± .25	3.33 ± .18	967 ± 62	6.65 ± .31	3.34 ± .19	29
K^-p	100	6.76 ± .18	3.17 ± .10	2247 ± 152			
K^+p	175	7.61 ± .37	3.85 ± .21	665 ± 74			
K^-p	175	7.56 ± .18	3.63 ± .11	1787 ± 100	7.33 ± .21	3.51 ± .15	30*
pp	100	6.44 ± .17	3.24 ± .13	1712 ± 113	6.37 ± .06	3.26 ± .05	26
$\bar{p}p$	100	6.52 ± .11	3.13 ± .09	2482 ± 93	6.74 ± .05	3.26 ± .05	28
pp	175	7.54 ± .15	3.71 ± .10	2739 ± 130			
$\bar{p}p$	175	7.36 ± .24	3.81 ± .17	1093 ± 80			

*Results at 147 GeV/c

Table V

Inelastic Charged Topology Cross Section Comparisons

Charged Prong	Reaction: 100 $\pi^+ p$ Ours (mb)	100 $\pi^+ p$ Ref. 26 (mb)	100 pp Ours (mb)	100 pp Ref. 26 (mb)	100 $\pi^- p$ Ours (mb)	100 $\pi^- p$ Ref. 27 (mb)	100 $\bar{p}p$ Ours (mb)	100 $\bar{p}p$ Ref. 28 (mb)
2	2.5±.9	2.4 ±.2	3.7± .9	4.9±.3	1.9 ±.6	2.0 ±.3	4.6 ± .6	3.6 ± .3
4	4.2±.5	4.7 ±.2	8.9± .9	7.3±.3	4.8 ±.4	4.8 ±.1	8.0 ± .7	8.1 ± .2
6	4.4±.6	4.8 ±.2	7.0± .9	7.0±.3	5.0 ±.5	5.2 ±.1	8.3 ± .9	8.3 ± .2
8	4.0±.8	3.6 ±.2	4.3±1.0	5.6±.2	3.9 ±.6	4.3 ±.1	4.9 ±1.1	6.9 ± .2
10	2.5±.8	2.6 ±.2	4.4± .8	3.7±.2	2.8 ±.6	2.5 ±.1	4.4 ±1.1	4.1 ± .1
12	1.6±.5	1.3 ±.1	1.7± .2	1.7±.1	1.7 ±.4	1.4 ±.1	3.0 ± .7	2.2 ± .1
14	.5±.1	.5 ±.1	.7± .2	.8±.1	.5 ±.1	.6 ±.04	.8 ± .4	.9 ± .1
16	.2±.1	.13±.03	.3± .1	.2±.04	.12±.10	.13±.03	.2 ± .1	.4 ± .04
18	.1±.1	.04±.02	.1± .05	.1±.02	.03±.01	.05±.01	.06± .06	.12± .02
20	------	.02±.01	--------	.1±.1	--------	.01±.008	---------	.04± .01
	20.0±.9	20.2±.2	31.3±1.2	31.4±.2	20.7±.7	21.0±.2	34.2±1.1	35.6±.4

Table VI

Inelastic Charged Topology Cross Section (mbarns)

Charged Prong	Reaction: +100 K^+p (mb)	-100 K^-p (mb)	+175 π^+p (mb)	+175 K^+p (mb)	+175 pp (mb)	-175 π^-p (mb)	-175 K^-p (mb)	-175 $\bar{p}p$ (mb)
2	1.7± .9	2.1± .5	1.9± .8	2.1±1.6	3.7± .8	2.2± .5	1.5±1.0	4.0±2.0
4	3.5± .5	3.8± .5	3.7± .7	2.6± .9	5.4± .8	3.7± .4	3.7± .5	6.8±1.2
6	3.8± .6	4.9± .7	4.2± .9	3.4±1.1	6.5±1.0	3.6± .5	3.4± .7	6.9±1.7
8	3.2± .6	2.9± .7	3.6±1.0	3.6±1.3	5.9±1.0	3.7± .6	3.7± .8	7.0±2.3
10	2.3± .5	2.8± .7	2.5±1.0	2.3±1.2	4.2±1.0	2.9± .4	2.7± .5	3.5±1.5
12	1.1± .5	1.3± .4	2.7± .7	1.5± .7	3.7± .8	1.7± .3	1.5± .3	3.3±1.5
14	.5± .1	.4± .2	1.0± .5	.5± .5	1.5± .2	1.0± .3	.8± .3	1.7± .5
16	.2± .1	.1± .1	.4± .3	-------	.6± .2	.6± .2	.5± .2	.9± .3
18	.1± .1	.05±.05	.1± .1	-------	.3± .1	.4± .1	.2± .1	.5± .3
20	-------	-------	-------	-------	.1±.06	.2± .1	.1± .1	.3± .2
22	-------	-------	-------	-------	-------	.13±.07	-------	-------
Total Inelastic Cross Section :	16.4±1.6	18.4±1.1	20.2±1.1	17.1±1.7	31.7±1.0	19.9± .7	18.1±1.1	34.9±1.6

Table VII

Corrections and Systematic Errors
for Average Inelastic Charged Multiplicity

Uncorrected $\pi^- p \to X$ average = 7.43 ± .10

Type of Monte Carlo Corrections	Correction	Uncertainty in Correction
A) Physics Effects		
Delta Ray Production	-.70	.10
γ Conversions in Target Region	-.29	.03
K^0_S Decays	-.10	.05
Λ^0 Decays	-.07	.02
Secondary Interactions	-.70	.05
B) Equipment Response Correction		
MC Efficiency* and pulse height errors	.10	.02
Wire Chamber Efficiency and tracking Algorithm Mistakes	.52	.10
MT and MS Efficiency* and Backward Loss of Solid Angle	.15	.03
C) Other Sources		
Elastic Cross Section Subtraction	.48	.06
Inelastic Two-Prong Loss	-.03	.03
Total Correction	-.64	±.17**

Final Corrected $\pi^- p \to X$ average = 6.79 ± .11

*Note that these corrections include γ-ray conversions in the counters.

**Total correction uncertainty is the uncertainty in each correction added in quadrature. Note that the final quoted error does not include the .17.

TABLE VIII.

Fit Parameters

$\langle n \rangle_x = A + B \ln M_x^2 + C|t|$

100 GeV/c Reactions
(Positive Incident Beam Particles)

Reaction*	A	B	C	χ^2/DF
$\pi^+ \to \pi^+$	-.71± .15	1.34±.04	.33± .11	85/32
$\pi^+ \to \pi^-$	.61± .89	1.06±.22	-.46± .53	7/6
$\pi^+ \to K^+$	-.39± .53	1.24±.14	.41± .27	47/32
$\pi^+ \to K^-$	.83±3.70	1.84±.91	1.08±1.32	8/5
$\pi^+ \to p$	.82±1.31	1.01±.35	.08± .31	20/17
$K^+ \to \pi^+$	-2.42±2.05	1.74±.50	.18±1.22	3/7
$K^+ \to K^+$	-.42± .46	1.29±.13	.19± .37	48/27
$p \to \pi^+$	-4.85±1.96	1.98±.42	.68± .51	37/15
$p \to p$	-.78± .16	1.36±.05	.42± .10	98/35

Kinematic Region Fitted

$.2 < |t| < 2.$ GeV^2

$10 < M_x^2 < 130$ GeV^2

*All reactions are on proton targets. For instance $\pi^+ \to \pi^+$ is shorthand for $\pi^+ p \to \pi^+ X$.

TABLE VIII.cont.

Fit Parameters

$\langle n \rangle_x = A + B \ln M_x^2 + C|t|$

175 GeV/c Reactions
(Positive Incident Beam Particles)

Reaction*	A	B	C	χ^2/DF
$\pi^+ \to \pi^+$	-0.38±0.26	1.27±.06	0.25±0.14	47/25
$\pi^+ \to \pi^-$	-4.80±3.90	2.03±.80	0.78±1.16	16/6
$\pi^+ \to K^+$	-0.31±0.50	1.31±.12	0.17±0.27	23/25
$\pi^+ \to K^-$	-9.60±4.60	2.98±.99	1.40±1.40	2/6
$\pi^+ \to p$	-0.80±0.62	1.45±.19	-0.00±0.36	28/18
$K^+ \to \pi^+$	-1.23±1.04	1.38±.26	1.46±0.62	10/15
$K^+ \to K^+$	0.70±0.46	1.04±.12	0.08±0.31	37/23
$p \to \pi^+$	-4.50±1.42	1.91±0.28	0.58±0.22	30/16
$p \to p$	-0.80±0.27	1.38±.07	0.56±0.14	51/24

Kinematic Region Fitted

$.2 < |t| < 2.\ GeV^2$

$15 < M_x^2 < 230\ GeV^2$

*All reactions are on proton targets. For instance $\pi^+ \to \pi^+$ is shorthand for $\pi^+ p \to \pi^+ X$.

Fit Parameters

$\langle n \rangle_x = A + B \ln M_x^2 + C|t|$

100 GeV/c Reactions
(Negative Incident Beam Particles)

Reaction*	A	B	C	χ^2/DF
$\pi^- \to \pi^-$	-0.11±0.16	1.20±.05	0.39±0.10	61/23
$\pi^- \to \pi^+$	-2.37±0.52	1.68±.13	-0.41±0.38	8/6
$\pi^- \to K^-$	-0.30±0.62	1.19±.15	0.61±0.22	22/25
$\pi^- \to K^+$	1.42±1.83	0.71±.48	1.15±0.84	8/6
$\pi^- \to \bar{p}$	-0.93±1.60	1.20±.41	0.46±0.29	20/14
$\pi^- \to p$	-3.46±1.60	2.25±.50	-0.58±0.56	7/9
$K^- \to \pi^-$	-6.10±3.10	2.50±.70	0.20±0.90	4/9
$K^- \to K^-$	1.83±0.62	0.94±.16	0.64±0.40	39/21
$p^- \to \pi^-$	-1.02±4.80	1.47±1.00	-2.01±1.26	11/9
$p^- \to p^-$	1.62±0.46	0.94±0.12	0.80±0.20	41/25

Kinematic Region Fitted

$.2 < |t| < 2.\ GeV^2$

$10 < M_x^2 < 130\ GeV^2$

*All reactions are on proton targets. For instance $\pi^- \to \pi^-$ is shorthand for $\pi^- p \to \pi^- X$.

FIGURE CAPTIONS

1. Non-magnetic vertex detector MT and MB are scintillators, MC counters and lucite cerenkov radiators, and PC1,2,3 and multiwire proportional chambers.

2. Vertex z distribution as calculated by beam counters and spectrometer chambers. The kinematics were P_b=100 Gev, P_s=60 GeV, angle=3.5 mrad.

3. Typical single MC counter pulse height showing particle topology cuts.

4. KNO scaling curve for h^-p reactions. The curve represents the KNO scaling fit for pp reactions of Ref. 17.

5. Typical t-dependence for leading particle reactions. The curves are fits described in Section IV., D.

6. Typical x-dependences for leading and production reactions. The curves are fits described in Section IV., D.

7. $\beta(x)$ for fits to $\bar{n} = \alpha(x) - \beta(x)t$ for leading particle reactions. The straight lines are trends from lower energy $pp \to px$ data (Ref. 21) and the arrow is the result of a global fit described in Sec. IV.

8. $\alpha(x)$ for $pp \to px$ at t=o. The solid line represents the fit described in Sec. IV.D. The dotted lines are the results of Ref. 20 and an average behavior of data compiled in Ref. 19.

9. $\alpha(x)$ for $\pi^{\pm}p \to \pi^{\pm}x$ at t=o. The solid line represents the fit described in Sec. IV.D. The dotted line represents the data of Ref. 19 for $\pi^- p \to \pi^- X$ at 147 GeV/c.

10. Average multiplicities for leading, resonance, and baryon excitation processes at M_x^2 = 53 GeV^2.

11. Average multiplicity for M_x^2 = 131 GeV^2 at 175 GeV and t=o. The total inelastic multiplicities are from fits to data compiled in Ref. 19.

12. $\ell n\, M_x^2$ or $\ell n\, s$ coefficients for the associated multiplicities.

13. Psuedo-rapidities of associated charged particles in the reaction $\pi^- p \to \pi^- X$ at 175 GeV, p_t=0.3 GeV/c.

14. Rapidity distributions for pp→px (this experiment), $\bar{p}p \to x$ (Ref. 23) and pp→X (Ref. 24) at a common $M_X^2 = 190\ GeV^2$.

15. Associated rapidity distributions for the reaction $\bar{p}p \to \pi^- X$.

16. Excess forward multiplicities for $n \geq 3.3$ at X=0.88.

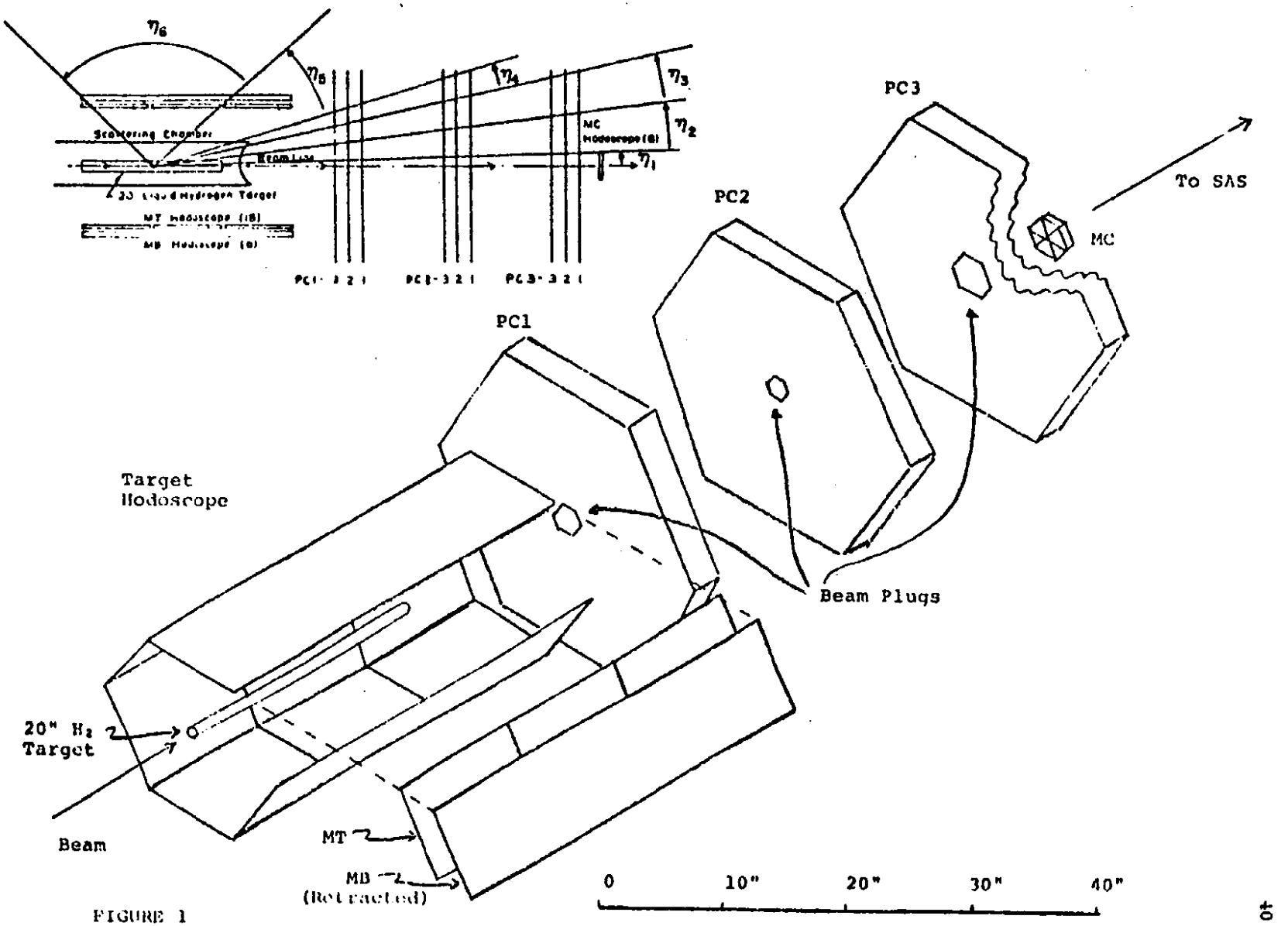
PC3
PC2
PC1
To SAS
MC
Target
Hodoscope
Beam Plugs
20" H2
Target
Beam
MT
MB
(Retracted)
0
10"
20"
30"
40"

FIGURE 1

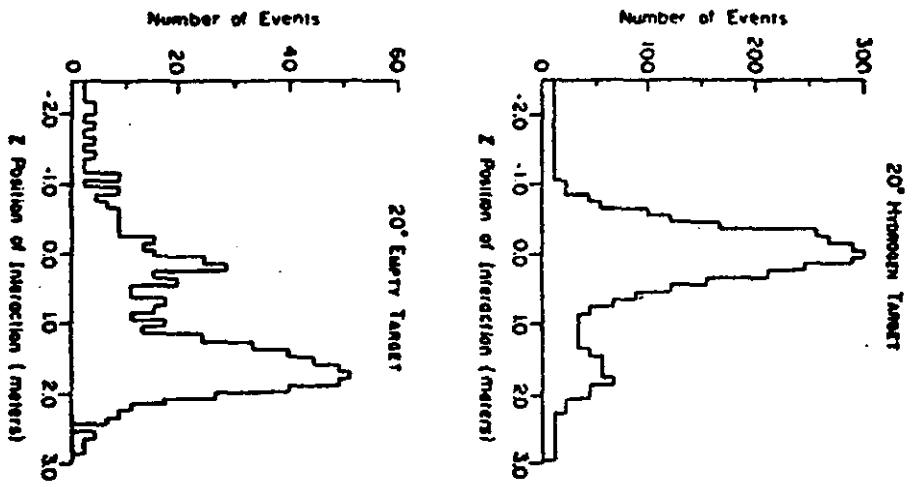

FIGURE 2

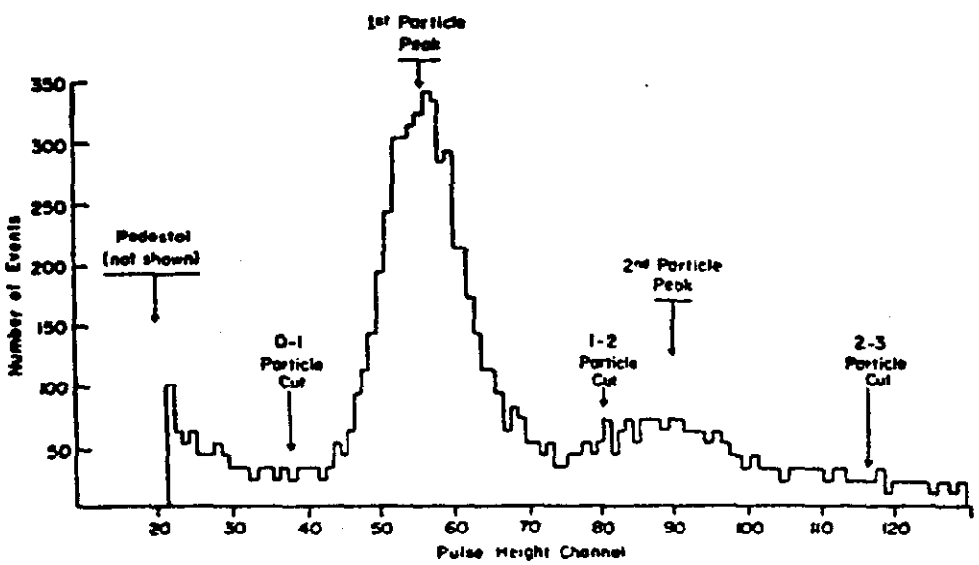

FIGURE 3

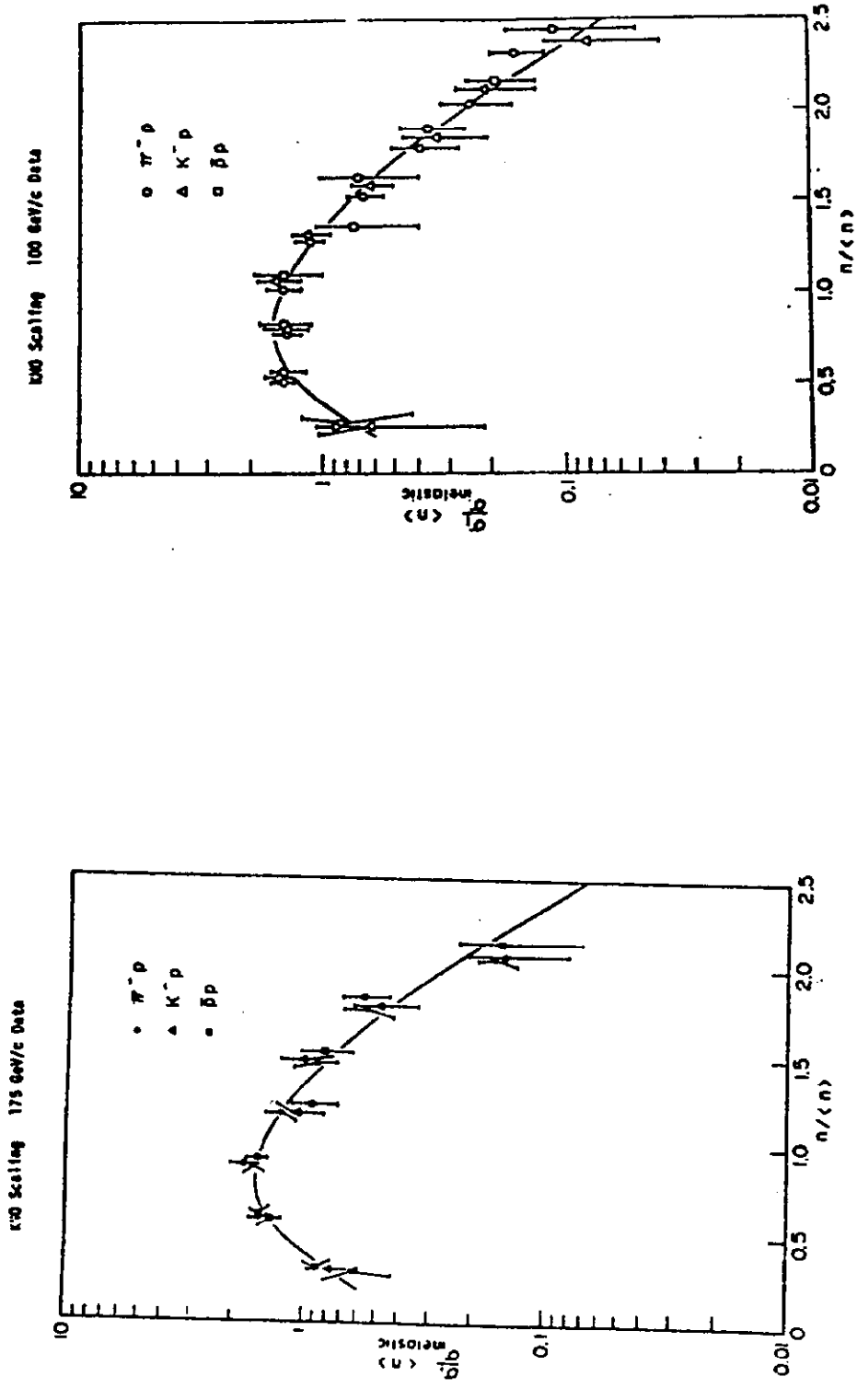
KNO Scaling 100 GeV/c Data
KNO Scaling 175 GeV/c Data
π⁻p
K⁻p
p̄p
n/⟨n⟩
⟨n⟩ ψ(z)
0.01
0.1
1
10
0
0.5
1.0
1.5
2.0
2.5

FIGURE 4

Average Associated Charged Multiplicity vs. $|t|$
for the Reaction $p + p \rightarrow p + X$ P_{Beam} = 175 GeV/c
at X_F = .94, .6, .3.

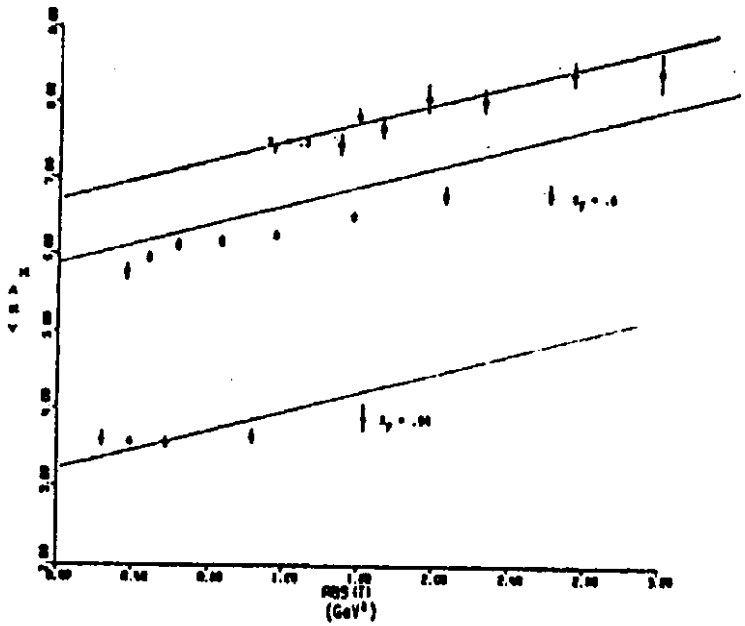

Average Associated Charged Multiplicity vs. $|t|$
for the Reaction $\pi^- + p \rightarrow \pi^- + X$ P_{Beam} = 100 GeV/c
at X_F = .92, .6, .3.

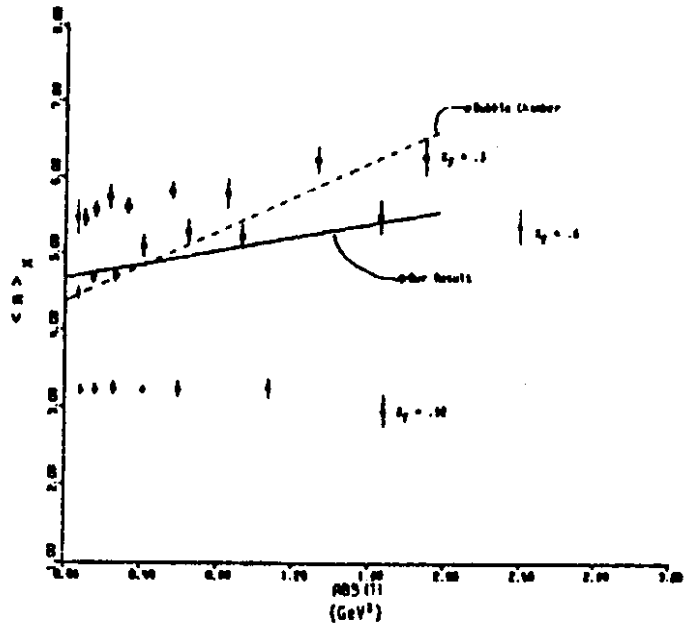

FIGURE 5

$p + p$ Average of the Associated Charged Multiplicity vs. X_F

$P_T = .5$ GeV/c

$P_{Beam} = 175$ GeV/c

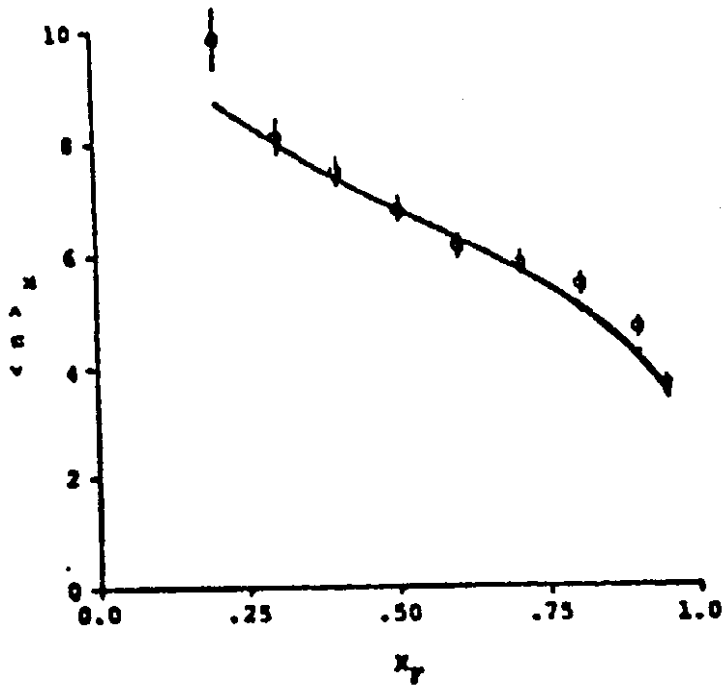

$\pi^+ + \pi^+$ Average of the Associated Charged Multiplicity vs. X_F

$P_T = .5$ GeV/c

$P_{Beam} = 100$ GeV/c

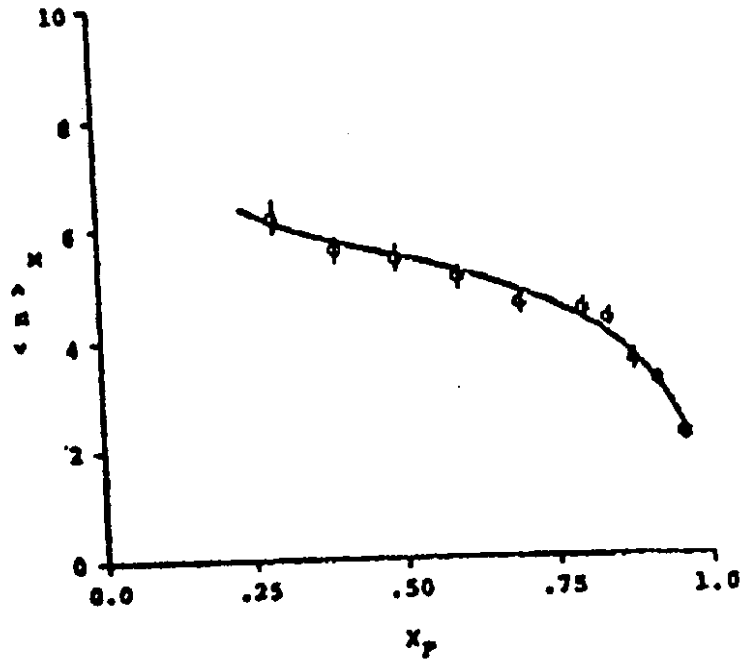

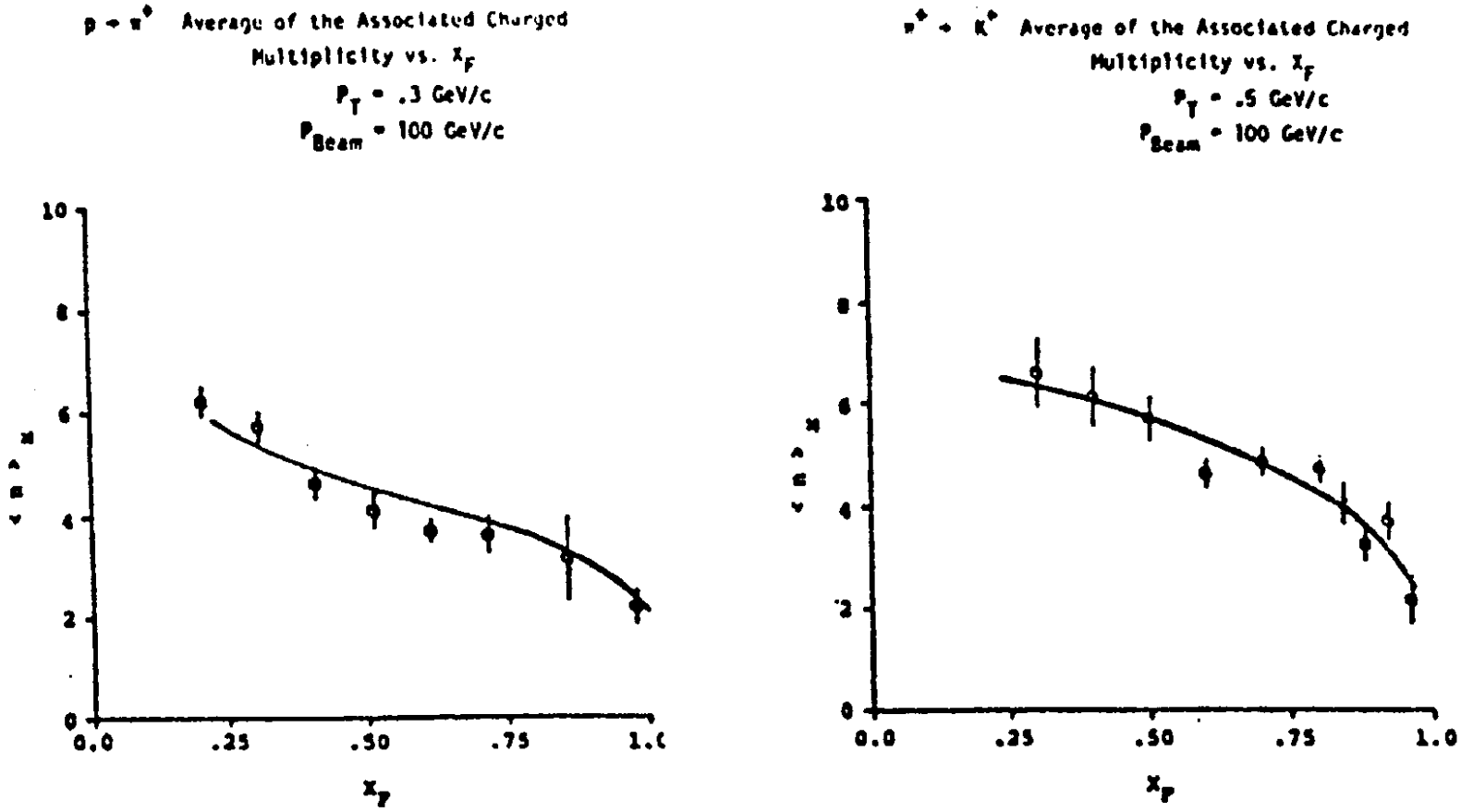
p + π⁺ Average of the Associated Charged Multiplicity vs. X_F
P_T = .3 GeV/c
P_{Beam} = 100 GeV/c
π⁺ + K⁺ Average of the Associated Charged Multiplicity vs. X_F
P_T = .5 GeV/c
P_{Beam} = 100 GeV/c
X_F
0.0
.25
.50
.75
1.0
0
2
4
6
8
10

FIGURE 6

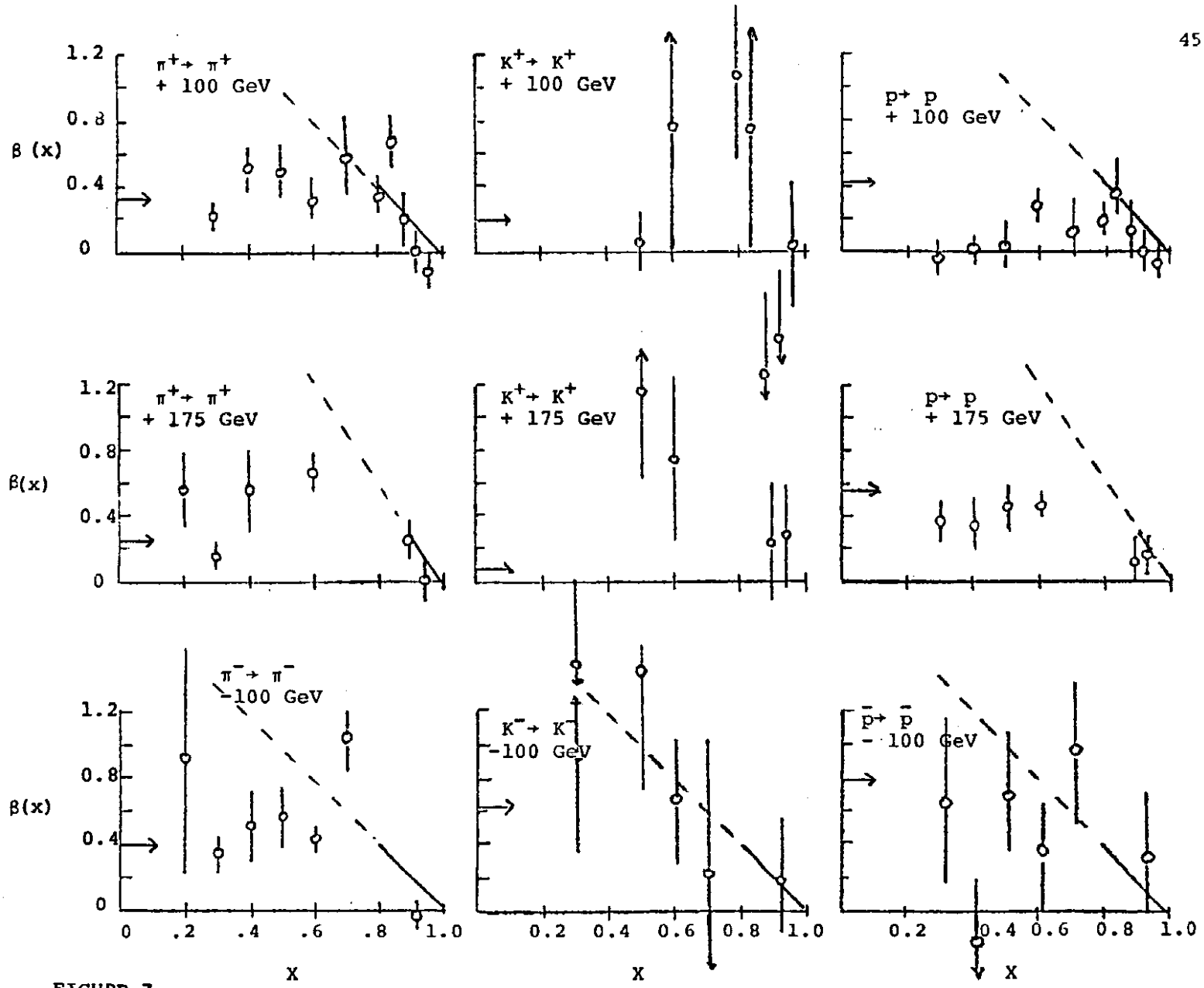
$\pi^+ \to \pi^+$ + 100 GeV
$K^+ \to K^+$ + 100 GeV
$p \to p$ + 100 GeV
$\pi^+ \to \pi^+$ + 175 GeV
$K^+ \to K^+$ + 175 GeV
$p \to p$ + 175 GeV
$\pi^- \to \pi^-$ -100 GeV
$K^- \to K^-$ -100 GeV
$\bar{p} \to \bar{p}$ - 100 GeV
β (x)
β(x)
β(x)
1.2
0.8
0.4
0
0 .2 .4 .6 .8 1.0
0.2 0.4 0.6 0.8 1.0
X

FIGURE 7

$a(x) = \langle n \rangle \Big|_{t=0}$

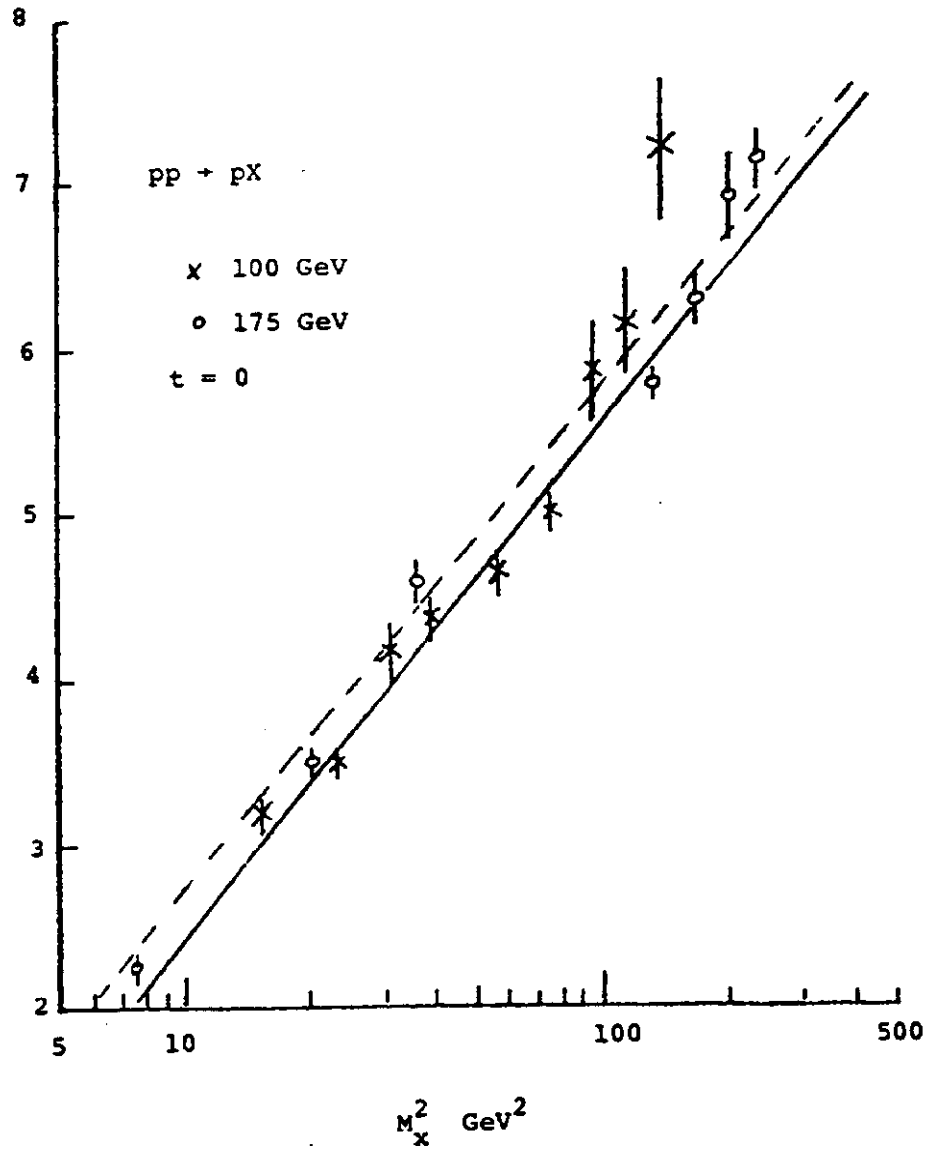

FIGURE 8

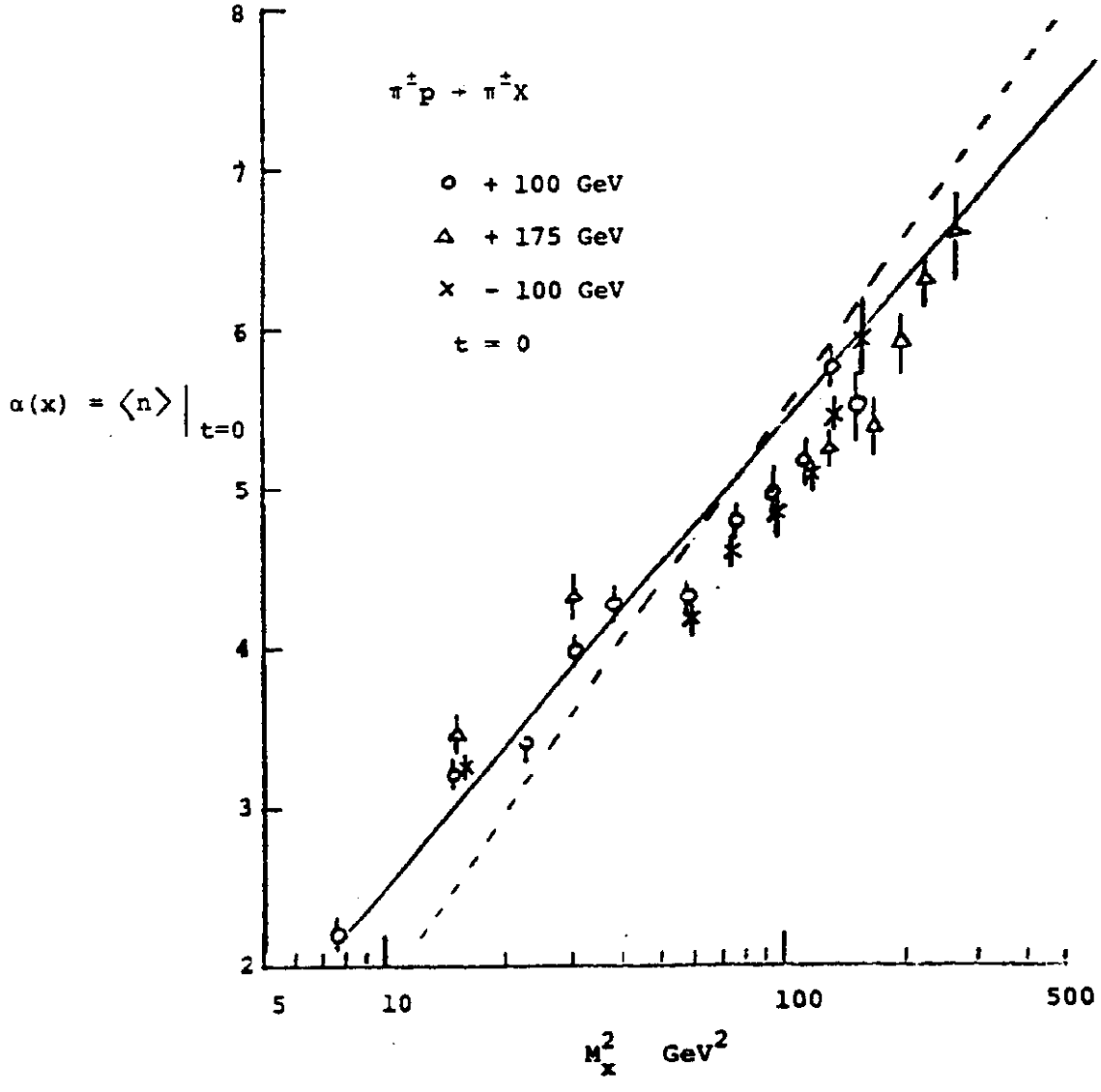
$\pi^{\pm}p \to \pi^{\pm}X$
o + 100 GeV
Δ + 175 GeV
× - 100 GeV
t = 0
$\alpha(x) = \langle n \rangle \Big|_{t=0}$
8
7
6
5
4
3
2
5
10
100
500
M_x^2 GeV^2

FIGURE 9

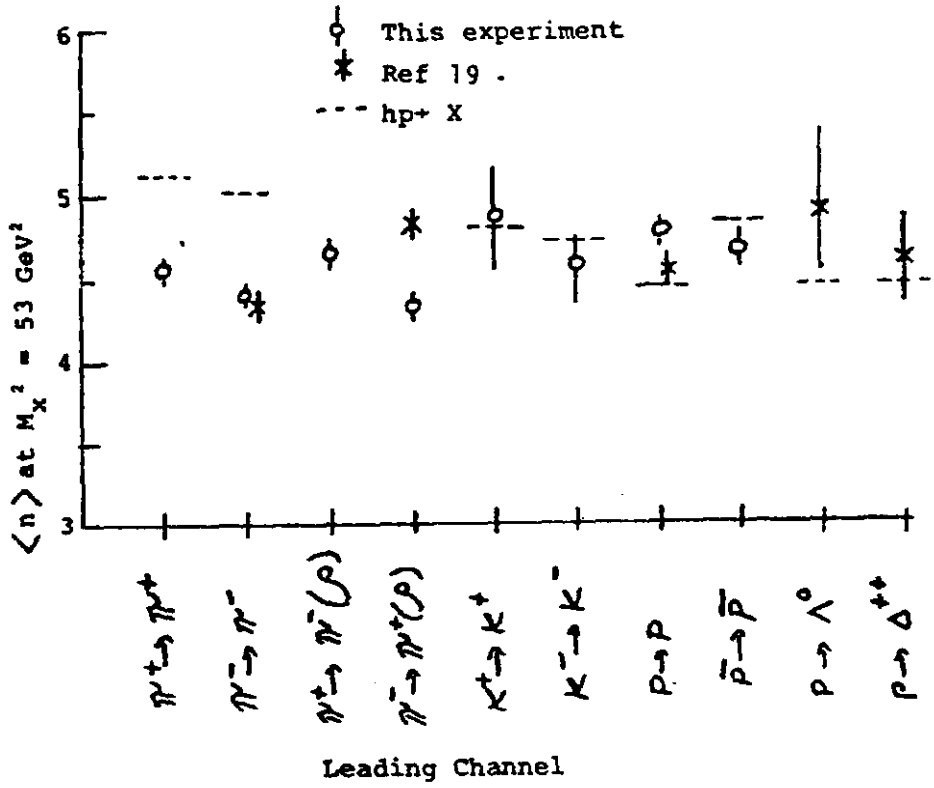
This experiment
Ref 19 .
hp+ X
6
5
4
3
⟨n⟩ at M_x^2 = 53 GeV²
$\pi^+ \to \pi^+$
$\pi^- \to \pi^-$
$\pi^+ \to \pi^-(\rho)$
$\pi^- \to \pi^+(\rho)$
$K^+ \to K^+$
$K^- \to K^-$
$p \to p$
$\bar{p} \to \bar{p}$
$p \to \Lambda^0$
$p \to \Delta^{++}$
Leading Channel

FIGURE 10

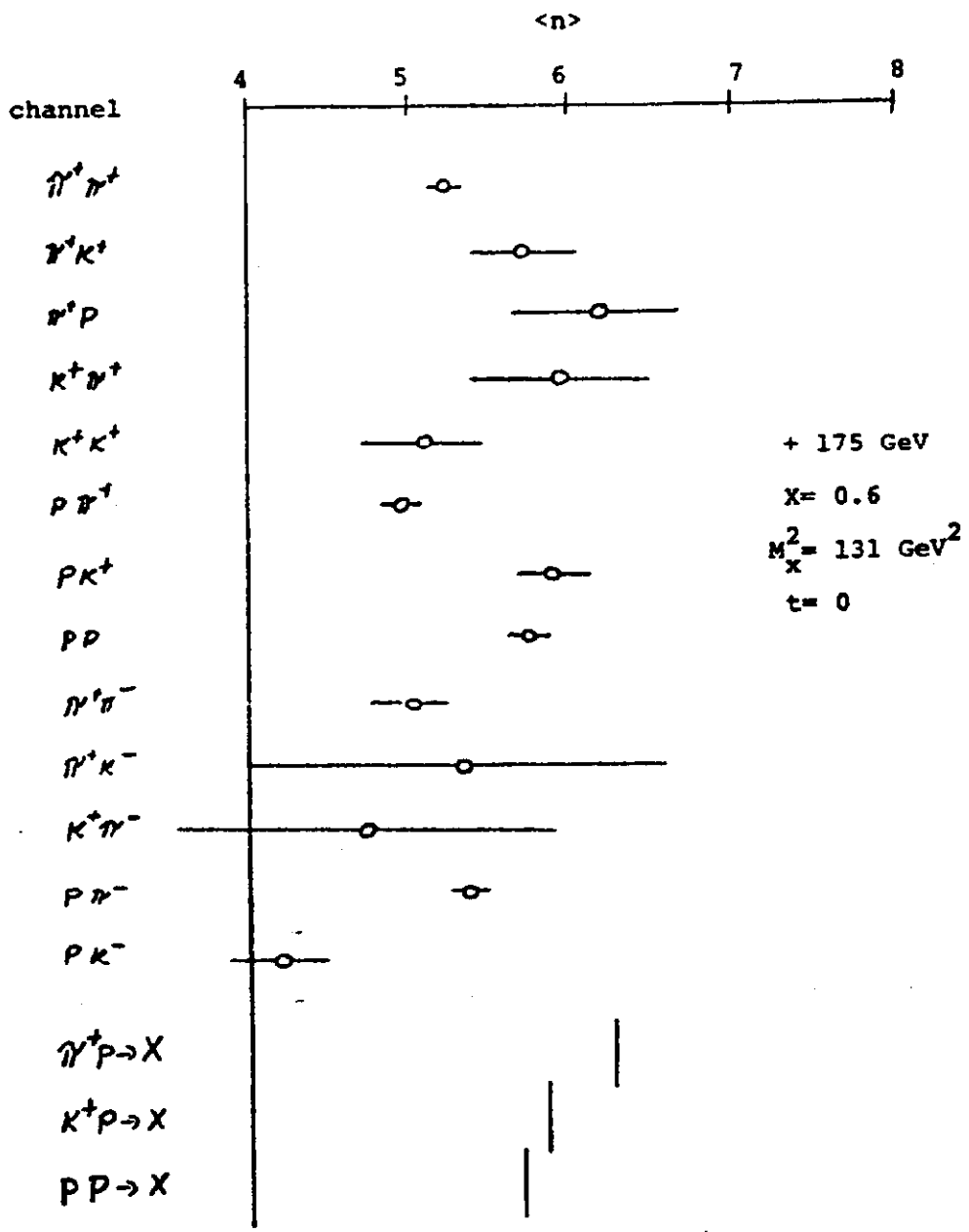
<n>
4
5
6
7
8
channel
$\pi^+\pi^+$
π^+K^+
π^+p
$K^+\pi^+$
K^+K^+
$p\pi^+$
pK^+
pp
$\pi^+\pi^-$
π^+K^-
$K^+\pi^-$
$p\pi^-$
pK^-
$\pi^+p\to X$
$K^+p\to X$
$pp\to X$
+ 175 GeV
X= 0.6
M_x^2= 131 GeV^2
t= 0

Figure 11.

Comparison of Coefficients of $\ell n\ M_x^2$ for Reactions a + p → a + X to the Coefficients of $\ell n\ s$ for Reactions a + p → X

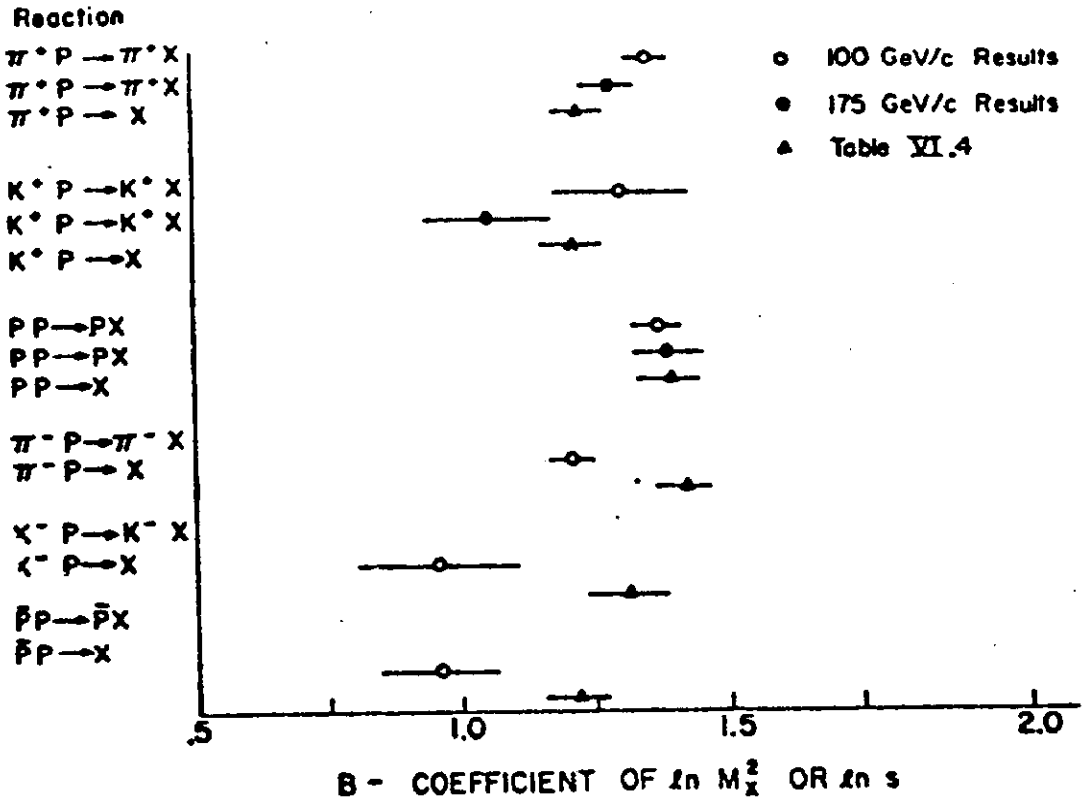

Figure 12.

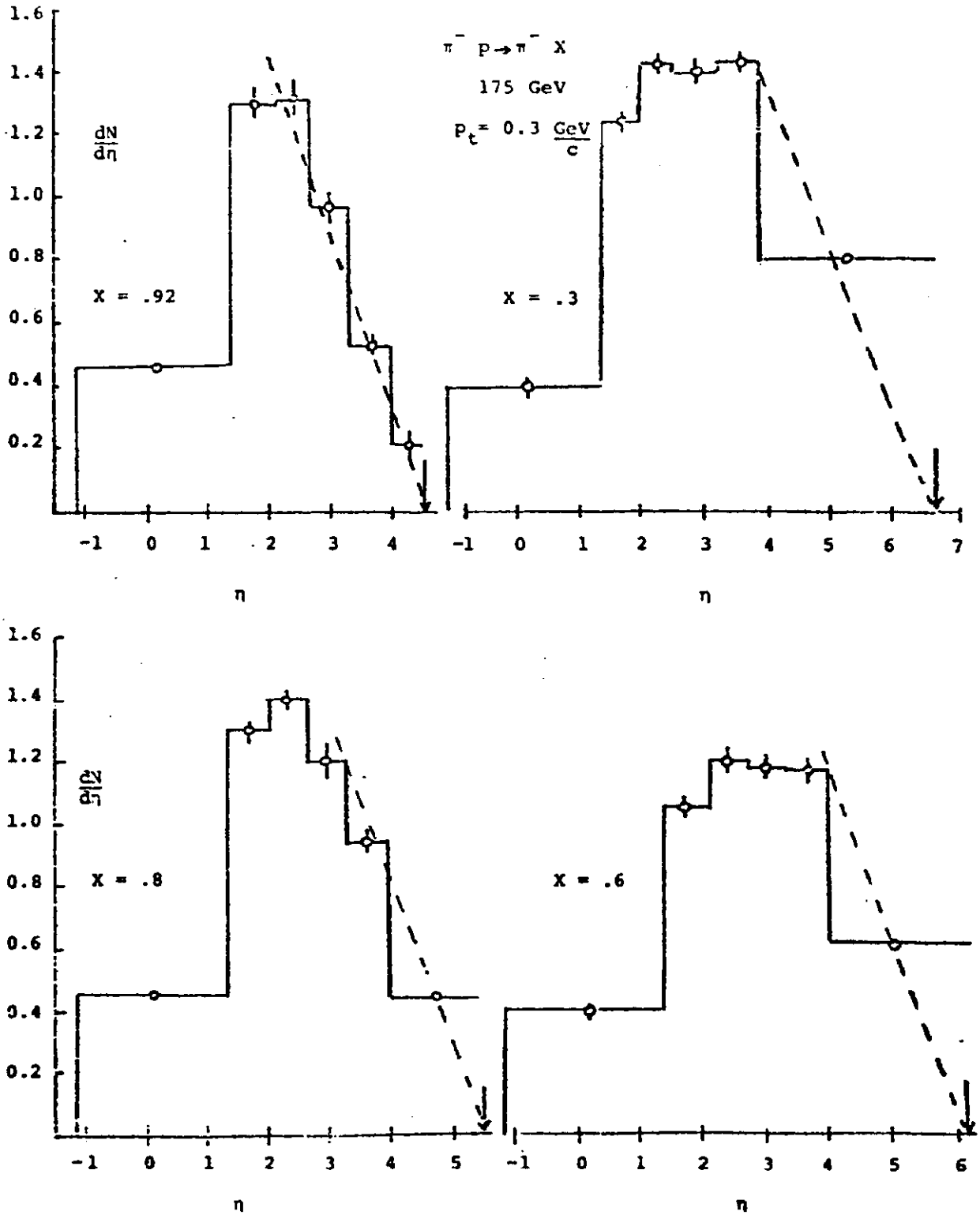

FIGURE 13

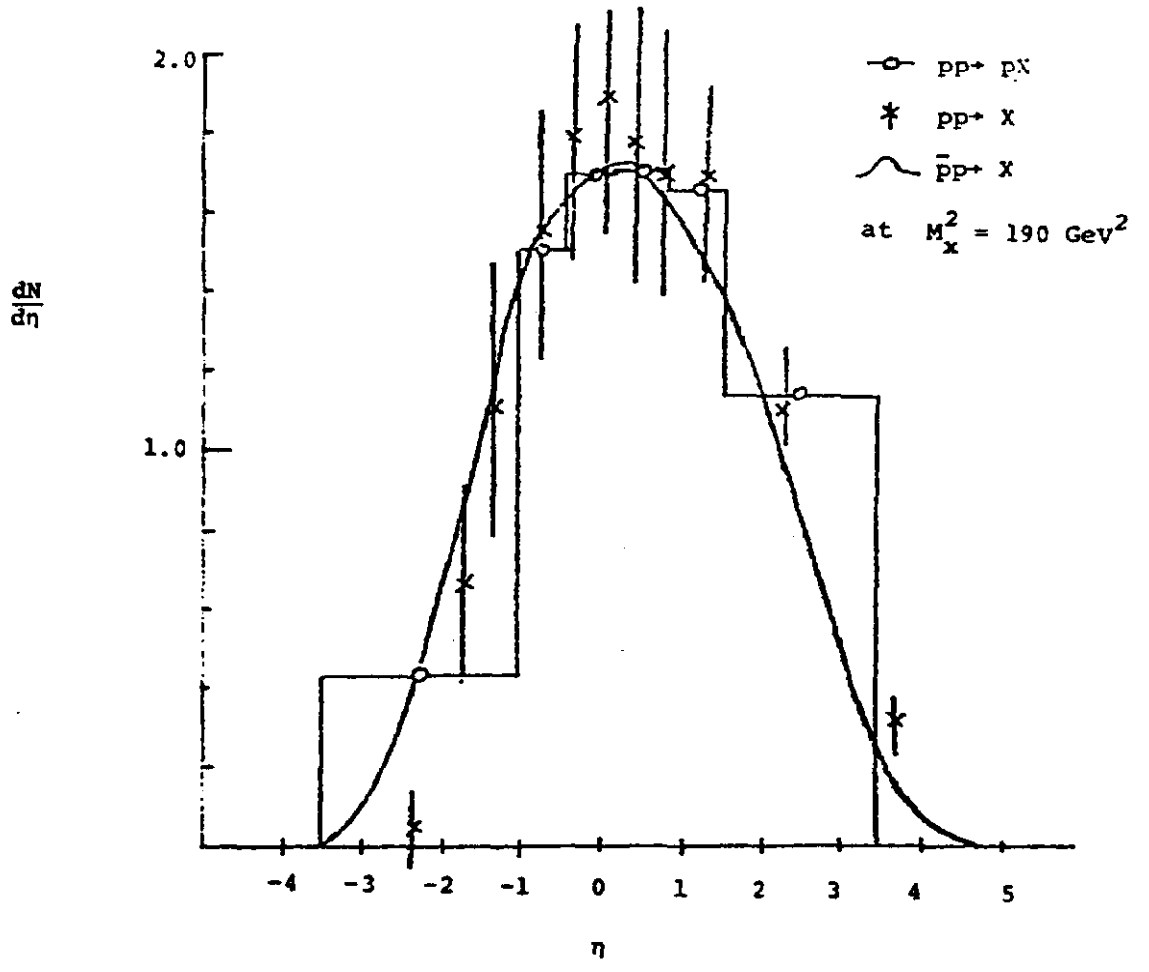

FIGURE 14

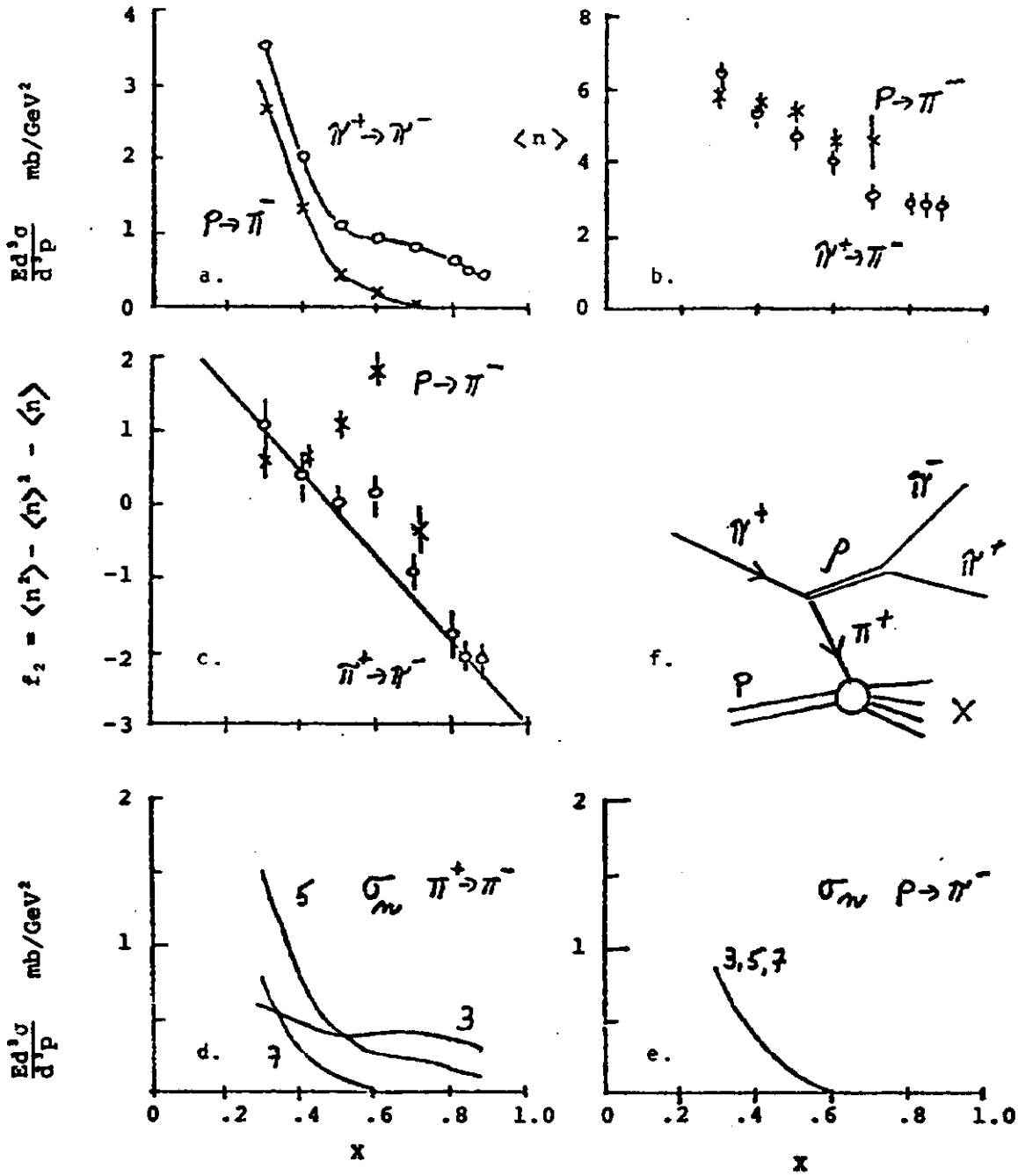
a.
b.
c.
d.
e.
f.
$\frac{Ed^3\sigma}{d^3p}$ mb/GeV²
$\langle n \rangle$
$f_2 = \langle n^2 \rangle - \langle n \rangle^2 - \langle n \rangle$
$p \to \pi^-$
$\pi^+ \to \pi^-$
$\sigma_{\pi\pi}$
3,5,7
x

FIGURE 15

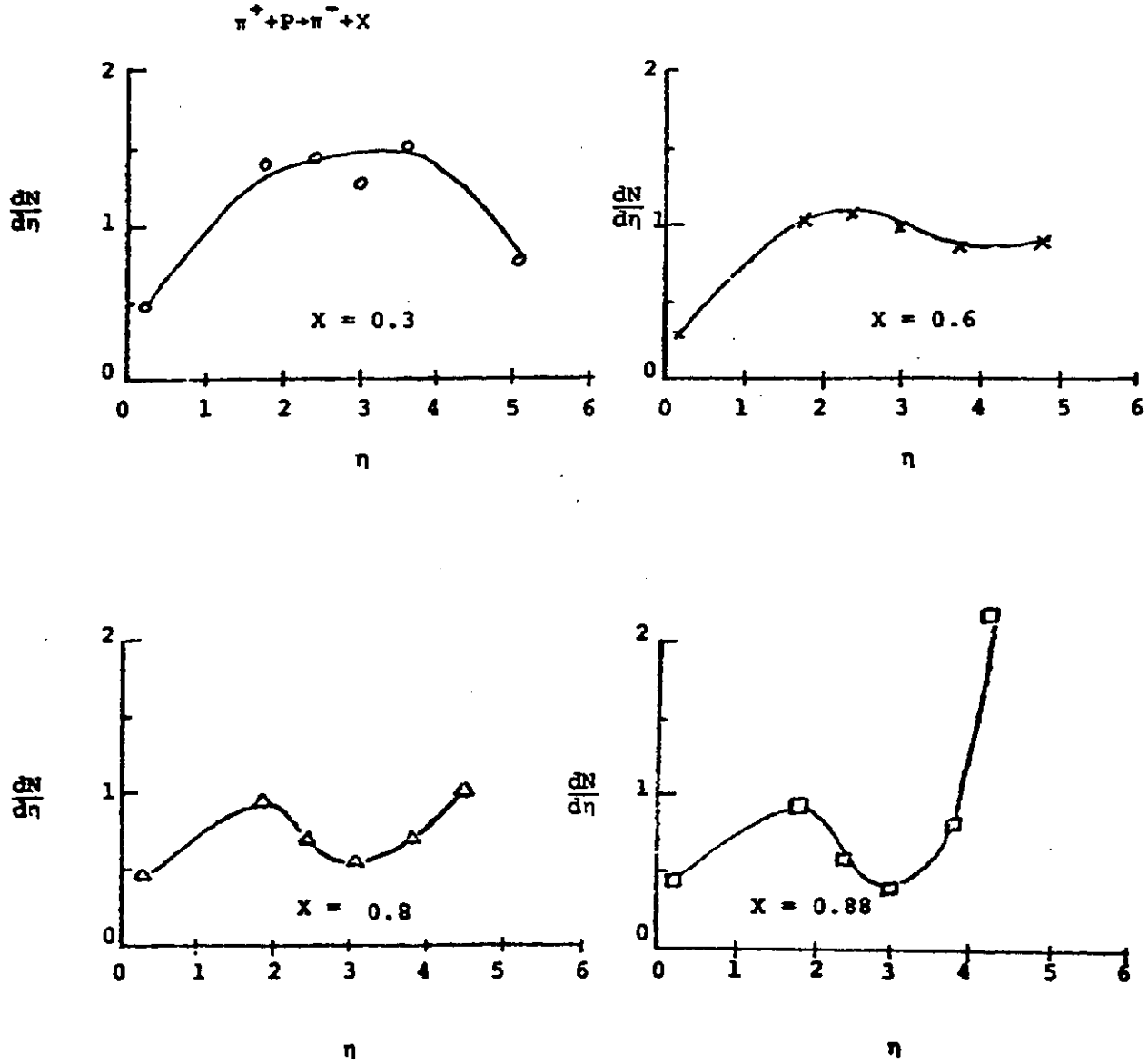

Figure 15 g.

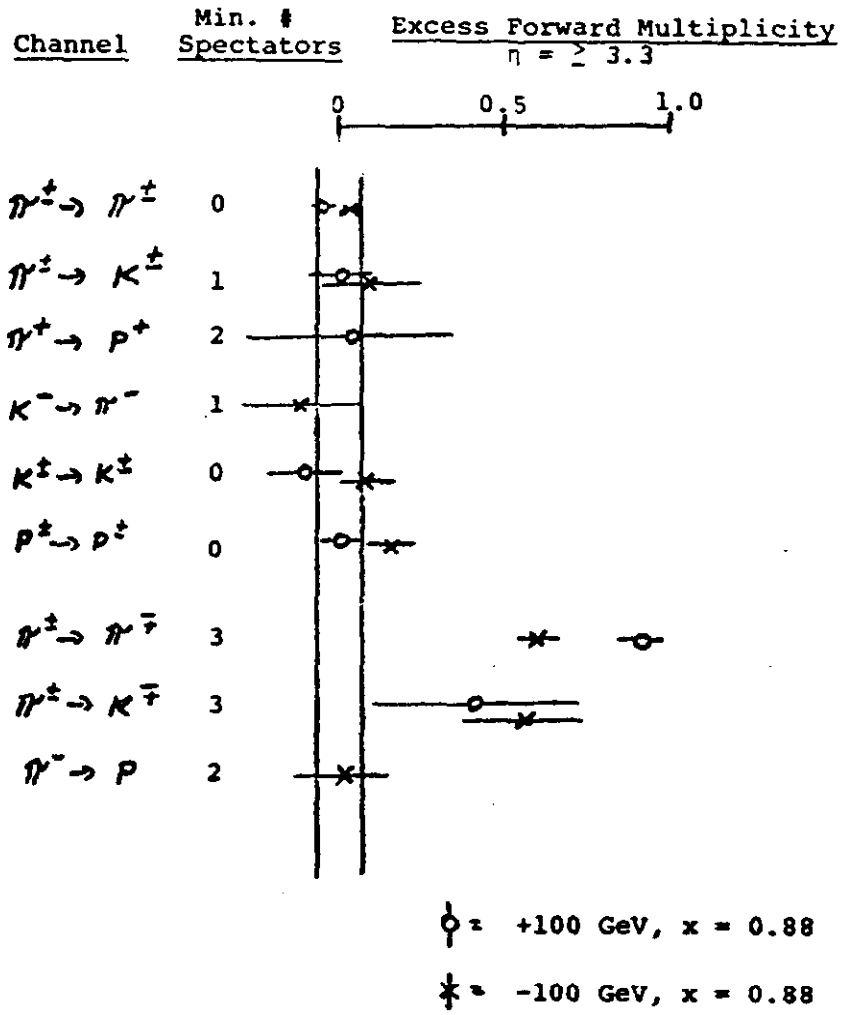
Channel
Min. # Spectators
Excess Forward Multiplicity
η = ≥ 3.3
0
0.5
1.0
π± → π±
0
π± → K±
1
π+ → p+
2
K− → π−
1
K± → K±
0
p± → p±
0
π± → π∓
3
π± → K∓
3
π− → p
2
= +100 GeV, x = 0.88
= −100 GeV, x = 0.88

FIGURE 16